

**Meta-analysis of Cryogenian through modern quartz microtextures reveals sediment transport histories**

**Jocelyn N. Reahl<sup>1,2</sup>, Marjorie D. Cantine<sup>1</sup>, Julia Wilcots<sup>1</sup>, Tyler J. Mackey<sup>1,3</sup>, Kristin D. Bergmann<sup>1</sup>**

*<sup>1</sup>Massachusetts Institute of Technology, Department of Earth, Atmospheric, and Planetary Sciences, Cambridge, Massachusetts, 02139, U.S.A.*

*<sup>2</sup>Now at the California Institute of Technology, Division of Geological and Planetary Sciences, Pasadena, California, 91125, U.S.A.*

*<sup>3</sup>Now at the University of New Mexico, Department of Earth and Planetary Sciences, Albuquerque, New Mexico, 87131, U.S.A.*

Corresponding author: Jocelyn N. Reahl (jreahl@caltech.edu)

1 **ABSTRACT**

2 Quantitative scanning electron microscopy (SEM) quartz microtextural analysis can  
3 reveal the transport histories of modern and ancient sediments. However, because workers  
4 identify and count microtextures differently, it is difficult to directly compare quantitative  
5 microtextural data analyzed by different workers. As a result, the defining microtextures of  
6 certain transport modes and their probabilities of occurrence are not well constrained. We used  
7 principal component analysis (PCA) to directly compare modern and ancient aeolian, fluvial, and  
8 glacial samples from the literature with 9 new samples from active aeolian and glacial  
9 environments. Our results demonstrate that PCA can group microtextural samples by transport  
10 mode and differentiate between aeolian and fluvial/glacial transport modes across studies. The  
11 PCA ordination indicates that aeolian samples are distinct from fluvial and glacial samples,  
12 which are in turn difficult to disambiguate from each other. Ancient and modern sediments are  
13 also shown to have quantitatively similar microtextural relationships. Therefore, PCA may be a  
14 useful tool to constrain the ambiguous transport histories of some ancient sediment grains. As a  
15 case study, we analyzed two samples with ambiguous transport histories from the Cryogenian  
16 Bråvika Member (Svalbard). Integrating PCA with field observations, we find evidence that the  
17 Bråvika Member facies investigated here includes aeolian deposition and may be analogous to  
18 syn-glacial Marinoan aeolian units including the Bakoye Formation in Mali and the Whyalla  
19 Sandstone in South Australia.

20  
21 **INTRODUCTION**

22 Scanning electron microscopy (SEM) quartz microtextural analysis reveals microscale  
23 features (microtextures) that are formed during transport (Krinsley and Takahashi 1962; Krinsley

24 and Doornkamp 1973; Bull 1981). Because different transport modes imprint specific suites of  
25 microtextures onto quartz grains, quartz microtextural analysis is a useful technique to  
26 understand the transport histories of modern and ancient sedimentary deposits (Kransley and  
27 Doornkamp 1973; Mahaney 2002; Vos et al. 2014). Quantitative quartz microtextural analysis,  
28 which treats microtextural data as a multidimensional statistical problem, is a particularly  
29 promising method to quantify the probabilities of occurrence of each microtexture in a specific  
30 transport mode (Mahaney et al. 2001; Říha et al. 2019). However, because workers identify and  
31 count microtextures differently—even for sand grains from the same depositional environment  
32 (Culver et al. 1983)—it is difficult to directly compare quantitative microtextural data analyzed  
33 by more than one worker in the same reference frame.

34 Here we use principal component analysis (PCA) to directly compare quantitative  
35 microtextural data from modern and ancient aeolian, fluvial, and glacial sediments across  
36 workers. Because experimental studies have shown that certain microtextures form in specific  
37 transport settings (Kransley and Takahashi 1962; Lindé and Mycielska-Dowgiałło 1980; Costa et  
38 al. 2012; Costa et al. 2013; Costa et al. 2017), we expect the PCA ordinations to distinguish  
39 aeolian, fluvial, and glacial sediments from each other regardless of worker. We also hypothesize  
40 that the modern and ancient samples will be quantitatively similar to each other in PCA space,  
41 and that the depositional histories of ambiguous ancient sedimentary environments can be  
42 constrained using this method.

43 One such case of an ambiguous ancient sedimentary environment is the Cryogenian  
44 (720–635 Ma) Bråvika Member (northeastern Svalbard, Norway). The Bråvika Member is a  
45 northward-thickening and coarsening-upward wedge of quartz arenite with lenses and beds of  
46 dolomite (Halverson et al. 2004). Since the Bråvika Member was first recognized as a unit by

47 Halverson et al. (2004), there have been three prevailing hypotheses for what depositional  
48 environment the Bråvika could represent:

49 1) a glaciofluvial outwash plain associated with the overlying Wilsonbreen Formation  
50 (Halverson et al. 2004), which is correlated with the Marinoan “Snowball Earth” pan-glaciation  
51 (Hoffman et al. 2012);

52 2) an aeolian depositional environment associated with either the glacial conditions of the  
53 Wilsonbreen Formation or the tropical equatorial conditions of the underlying upper Elbobreen  
54 Formation (Halverson 2011), the latter of which is correlated with the Cryogenian interglacial  
55 period (Fairchild et al. 2016); or

56 3) a tropical fluvial environment associated with the upper Elbobreen Formation  
57 (Hoffman et al. 2012).

58 To test if our PCA analysis method can constrain the transport histories of ambiguous  
59 ancient sedimentary environments, we transformed two microtextural samples of the Bråvika  
60 Member from Buldrevågen (north-northeast Spitsbergen) into the PCA ordinations. Integrating  
61 the microtextural data with field observations from Buldrevågen, Geerabukta (Ny Friesland), and  
62 Gimleodden (Nordaustlandet), we show that PCA is not only able to distinguish aeolian, fluvial,  
63 and glacial transport modes from each other using microtextural data, but it is also able to help  
64 elucidate the ambiguous transport histories of ancient sediment grains.

65

66

## MATERIALS

67

### *Modern Samples*

68

69

**New Modern Samples.** — We present five new aeolian samples from the McMurdo  
Dry Valleys (Antarctica), Algodones Dunes of California (Cocopah (*Kwapa*), Kumeyaay, Salt

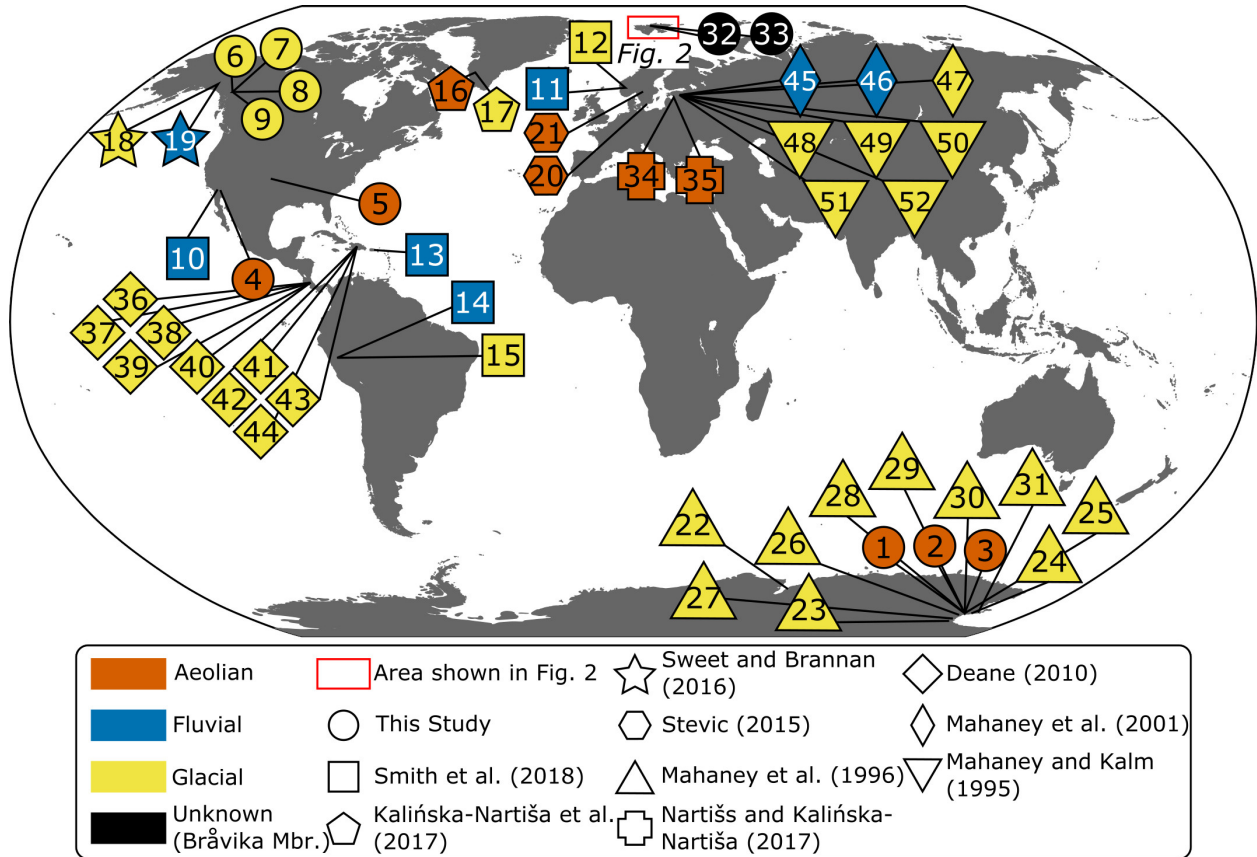


**Figure 1.** Global map of all samples analyzed in this study. The number in each marker corresponds to the sample group number in Tables 1 and 2.

70 River Pima-Maricopa (*O’odham-Piipaash*), and Quechan (*Kwatsáan*) territory), and Waynoka  
 71 Dunes of Oklahoma (Comanche (*N̄m̄m̄m̄m̄*), Keechi (*Ki:che:ss*), Kiowa (*[Gáui[dòñ:gyà]*), Osage  
 72 (*Wahzhazhe*), Tawakoni (*Tawá:kharih*), Waco (*Wi:ko?*), and Wichita (*Kirikir?i:s*) territory), as  
 73 well as four new glacial samples from the Llewellyn Glacier in British Columbia on Taku River  
 74 Tlingit (*Lingít*) territory (Fig. 1; Table 1). Each of these samples are briefly described in the  
 75 following paragraphs, and more detailed descriptions can be found in the Supplementary  
 76 Material.

77 Of the five aeolian samples, three are sourced from perennially ice-covered lakes in the  
 78 McMurdo Dry Valleys: one from Lake Fryxell (documented in Jungblut et al. 2016), one from

**Table 1.** List of the samples from modern depositional environments considered in this study. Each group of samples is assigned a number for later reference in Figures 1 and 5 (Column #). Column S indicates the number of samples in each sample group, and column N indicates the number of quartz grains in each sample group.

Study	#	Sample Location	Transport	S	N	GPS Point
This Study	1	Lake Fryxell, McMurdo Dry Valleys, Antarctica	Aeolian	1	31	77°36'48"S, 163°06'40"E
	2	Lake Joyce, McMurdo Dry Valleys, Antarctica	Aeolian	1	34	77°43'11"S, 161°36'25"E
	3	Lake Vanda, McMurdo Dry Valleys, Antarctica	Aeolian	1	30	77°31'38"S, 161°36'24"E
	4	Algodones Dunes, California, U.S.	Aeolian	1	44	33°08'57"N, 115°18'48"W
	5	Waynoka Dunes, Oklahoma, U.S.	Aeolian	1	48	36°33'35"N, 98°53'56"W
	6	Llewellyn Glacier, B.C. (JIF19-C26-01)	Glacial	1	31	59°00'49"N, 134°07'15"W
	7	Llewellyn Glacier, B.C. (JIF19-C26-02)	Glacial	1	39	59°00'48"N, 134°07'13"W
	8	Llewellyn Glacier, B.C. (JIF19-C26-03)	Glacial	1	36	59°00'48"N, 134°07'13"W
	9	Llewellyn Glacier, B.C. (JIF19-C26-04)	Glacial	1	40	59°00'50"N, 134°07'14"W
Smith et al. (2018)	10	Anza-Borrego Desert, California, U.S.	Fluvial	5	250	32°54'00"N, 116°16'00"W
	11	Auster and Storelvi Rivers, Norway	Fluvial	7	346	61°32'00"N, 06°57'00"E
	12	Austerdal Glacier Moraine, Norway	Glacial	1	50	61°32'00"N, 06°57'00"E
	13	Rio Guayanés, Puerto Rico	Fluvial	6	297	18°03'00"N, 65°54'00"W
	14	Rio Parón, Peru	Fluvial	5	250	09°00'00"S, 77°42'00"W
Kalińska-Nartiša et al. (2017)	15	Moraine Proximal to Lake Parón, Peru	Glacial	1	48	09°00'00"S, 77°42'00"W
	16	Russell Glacier, Greenland (CE1, CE2, CE8)	Aeolian	3	60	67°05'00"N, 50°20'00"W
Sweet and Brannan (2016)	17	Russell Glacier, Greenland (CE12, CE13)	Glacial	2	40	67°07'00"N, 50°05'00"W
	18	Chitina Glacier Moraine to 12 km Past Tana River Confluence, Alaska, U.S. (CR-1 to CR-23)	Glacial	22	626	61°05'44"N, 142°11'03"W
Stevic (2015)	19	12 km Past Tana River Confluence to the Copper River, Alaska, U.S. (CR-24 to CR-41)	Fluvial	18	450	61°21'42"N, 143°46'34"W
	20	Coastal Sand Dune, Vittskövle, Sweden	Aeolian	1	15	55°51'56"N, 14°10'02"E
Mahaney et al. (1996)	21	Inland Sand Dune, Brattforsheden, Sweden	Aeolian	1	15	59°36'26"N, 13°53'03"E
	22	Lichen Valley, Vestfold Hills, Antarctica (Site A)	Glacial	1	25	68°28'53"S, 78°10'24"E
	23	Ackerman Ridge, Scott Glacier area, Antarctica (Sites B – C)	Glacial	1	25	85°45'00"S, 153°00'00"W
	24	Southern Inexpressible Island, Antarctica (Site D)	Glacial	1	25	74°54'00"S, 163°39'00"E
	25	Taylor Glacier, McMurdo Dry Valleys, Antarctica (Site E)	Glacial	1	25	77°44'00"S, 162°10'00"E
	26	Hatherton Glacier, Antarctica (Site F)	Glacial	1	25	79°55'00"S, 157°35'00"E
	27	Roberts Massif, Antarctica (Sites G – H)	Glacial	2	50	85°32'00"S, 177°05'00"W
	28	Barwick Valley, Antarctica (Site I)	Glacial	1	25	77°23'24"S, 161°02'18"E
	29	Cambridge Glacier, Antarctica (Site J)	Glacial	1	25	76°57'00"S, 160°31'00"E
	30	Southern Inexpressible Island, Antarctica (Site D)	Glacial	1	25	75°38'00"S, 161°05'00"E
	31	Luther Peak Basin, Edisto Inlet, Antarctica (Site L)	Glacial	1	25	72°22'00"S, 169°50'00"E

79 Lake Joyce (documented in Mackey et al. 2015) and one from Lake Vanda (documented in  
80 Mackey et al. 2017). The bulk of coarse-grained sedimentation under the ice cover of these lakes  
81 is wind-blown quartz- and feldspar-rich sand that melts through the ice and is deposited within  
82 layers of microbial mats on the lake floor (Gumbley 1975; Green et al. 2004; Shacat et al. 2004;  
83 Jungblut et al. 2016). The lakes' lack of wind-driven turbulence (Spigel and Priscu 1998) and  
84 neutral to high pH (Green et al. 2004; Shacat et al. 2004; Jungblut et al. 2016) suggest that these  
85 aeolian grains are negligibly overprinted by lacustrine transport or acidification processes after  
86 they melt through the ice.

87         The remaining two aeolian samples are from the Algodones Dunes and the Waynoka  
88 Dunes (both documented by Adams 2018; Adams and Soreghan 2020). Both dunefields are  
89 sourced from fluvial deposits (Winspear and Pye 1995; Lepper and Scott 2005) and have been  
90 active since the late Holocene (Stokes et al. 1997; Lepper and Scott 2005). Given that aeolian  
91 transport over short distances and timeframes rapidly imprints aeolian microtextures on quartz  
92 grains (Costa et al. 2013), we expect there to be negligible fluvial overprinting on these samples.

93         The four glacial samples from the Llewellyn Glacier on the Juneau Icefield were  
94 collected from lateral glacial moraines (JIF19-C26-02 and JIF19-C26-03) and an ephemeral  
95 glaciofluvial melt stream 10 m downstream from a separated branch of ice from the Llewellyn  
96 Glacier (JIF19-C26-01 and JIF19-C26-04; Fig. S1). Because many kilometers of fluvial transport  
97 are needed to create a fluvial microtextural overprint on glacial sediment (Pippin 2016; Sweet  
98 and Brannan 2016; Křížek et al. 2017), samples JIF19-C26-01 and JIF19-C26-04 are more  
99 representative of a glacial setting than a fluvial setting.

100         **Modern Literature Samples.** — Previously published aeolian, fluvial, and glacial  
101 samples comprise the remainder of modern samples considered in this study (Fig. 1; Table 1).

102 We selected 5 studies to use in this modern dataset: Mahaney et al. (1996), Stevic (2015), Sweet  
103 and Brannan (2016), Kalińska-Nartiša et al. (2017), and Smith et al. (2018).

104 Mahaney et al. (1996) analyzed 11 glacial samples distributed around the Antarctic  
105 continent. Stevic (2015) analyzed two aeolian samples, one from a coastal dune in Vittskövle,  
106 Sweden and another from an inland sand dune near Brattforsheden, Sweden. Sweet and Brannan  
107 (2016) investigated the microtextural transition from glacially-dominated samples to fluvially-  
108 dominated ones using 46 samples of sand collected along a transect from the Chitina Glacier to  
109 the Copper River in Alaska. For the purposes of sorting these samples into *glacial* and *fluvial*  
110 bins, we use Sweet and Brannan's (2016) 5-point averaged fluvial-glacial (F/G) microtextural  
111 ratio. Samples with a 5-point averaged F/G > 1 are classified as *fluvial* samples and samples with  
112 a 5-point averaged F/G < 1 are classified as *glacial*. Kalińska-Nartiša et al. (2017) analyzed three  
113 aeolian samples and two glacial samples from the Russell Glacier in southwest Greenland.  
114 Finally, Smith et al. (2018) analyzed 25 fluvial and glacial samples from the Anza-Borrego  
115 Desert in California, the Auster and Storelvi Rivers in Norway, the Rio Guayanés in Puerto Rico,  
116 and the Rio Parón in Peru. Because Smith et al. (2018) saw no significant change in percussion  
117 features along each of the river transects—even in glaciofluvial settings—the *fluvial* samples in  
118 Smith et al. (2018) are defined as those collected along river transects and the *glacial* samples  
119 are defined as those collected at moraines.

120

### 121 *Ancient Samples*

122 **Cryogenian Bråvika Member, Svalbard, Norway.** — We analyzed two samples of  
123 the Bråvika Member from a site at Buldrevågen in north-northeast Spitsbergen (Fig. 2), one at 12  
124 m and another at 22 m above the base of the Bråvika Member. We will present field observations

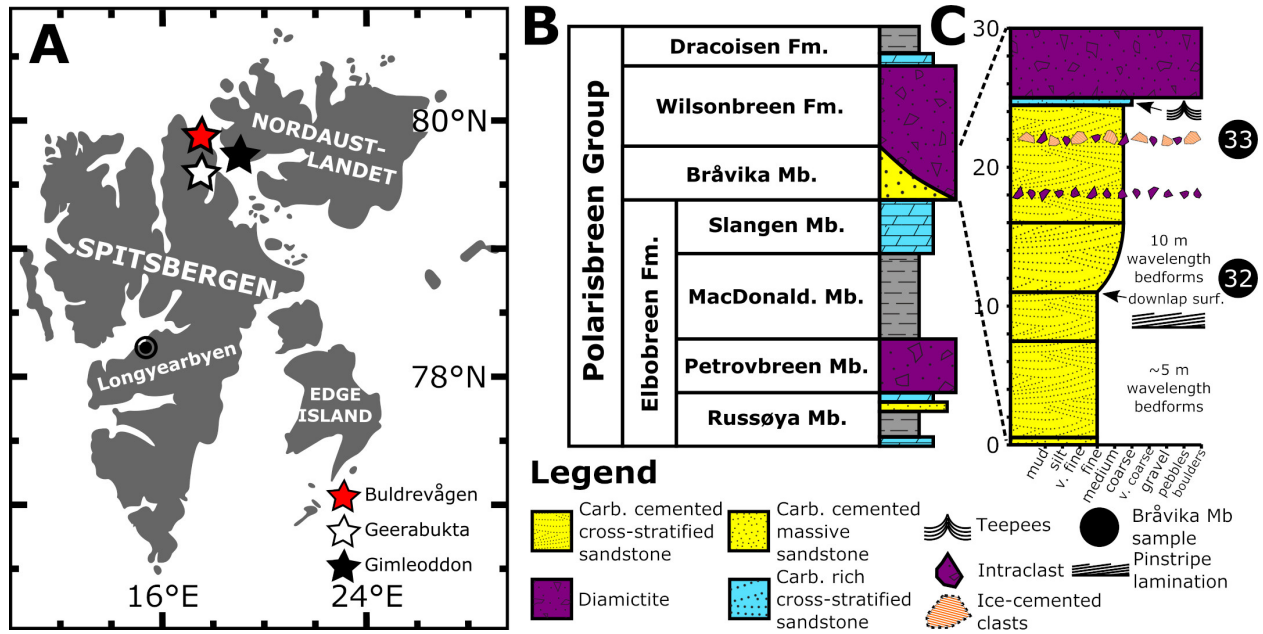


**Figure 2.** Geologic context and stratigraphy of the Cryogenian Bråvika Member in Svalbard. A) Map of the Svalbard archipelago. Each star indicates a site observed in this study: Buldrevågen (red), Geerabukta (white), and Gimleodden (black). B) Generalized stratigraphic nomenclature for the Cryogenian Polaribreen Group in Svalbard after Halverson et al. (2018). As shown here, the Bråvika Member is assigned to neither the Wilsonbreen nor the Elbobreen formations, as its assignment is a key question explored in this study. The Petrovbreen Member is correlated with the Sturtian pan-glaciation and the Wilsonbreen Formation is correlated with the Marinoan pan-glaciation (Hoffman et al. 2012). The MacDonaldryggen and Slangen members are correlated with the Cryogenian interglacial (Fairchild et al. 2016). C) Stratigraphic column of the Bråvika Member at Buldrevågen. The black circles indicate where samples 32 (J1701-156) and 33 (J1701-166) were collected for microtextural analysis.

125 of the Bråvika Member from outcrops in Buldrevågen, Geerabukta (Ny Friesland), and  
 126 Gimleodden (Nordautlandet) as context for the microtextural samples.

127 The Cryogenian Bråvika Member is a northward-thickening and coarsening-upward  
 128 wedge of quartz arenite with lenses and beds of dolomite that outcrop in northeastern Svalbard,  
 129 Norway (Halverson et al. 2004). The Bråvika Member is situated between two units that are  
 130 interpreted to represent different Cryogenian climate states (Fig. 2). The underlying siltstone and  
 131 dolomite of the upper Elbobreen Formation (MacDonaldryggen and Slangen Members) are

132 correlated with the warm Cryogenian interglacial period (Fairchild et al. 2016), which spanned  
133 from the Sturtian deglaciation to the Marinoan glacial initiation. Absolute age constraints on this  
134 period are limited, but the Sturtian deglaciation is constrained between  $>662.7 \pm 6.2$  Ma (U-Pb  
135 SIMS in South China; Yu et al. 2017) to  $>657.2 \pm 2.4$  Ma (Re-Os in Southern Australia; Kendall  
136 et al. 2006), and the Marinoan glacial onset is constrained between  $<654.6 \pm 3.8$  Ma (U-Pb SIMS  
137 in South China; Zhang et al. 2008) to  $>639.29 \pm 0.26/0.31/0.75$  Ma (U-Pb CA-ID-TIMS in  
138 Congo; Prave et al. 2016). The overlying glacial diamictites of the Wilsonbreen Formation share  
139 a reciprocal thickness relationship with the Bråvika Member and are correlated with the  
140 Marinoan glaciation (Hoffman et al. 2012), which ended between  $636.41 \pm 0.45$  Ma (U-Pb CA-  
141 ID-TIMS in Southern Australia; Calver et al. 2013) and  $635.2 \pm 0.6$  Ma (U-Pb zircon in South  
142 China; Condon et al. 2005).

143 **Ancient Literature Samples.** — In addition to the two Bråvika Member samples, we  
144 compiled a set of ancient aeolian, fluvial, and glacial microtextural samples from 4 studies:  
145 Mahaney and Kalm (1995), Mahaney et al. (2001), Deane (2010), and Nartišs and Kalińska-  
146 Nartiša (2017) (Fig. 1; Table 2).

147 Mahaney and Kalm (1995) analyzed 23 glacial samples from the Pleistocene Dainava,  
148 Ugandi, Varduva, and Latvia Tills in Estonia. Mahaney et al. (2001), following Mahaney and  
149 Kalm (2000), used quantitative microtextural analysis and Euclidian distances to characterize 29  
150 Pleistocene glacial samples, 3 Pleistocene glaciofluvial samples, and 21 Middle Devonian fluvial  
151 samples from Estonia. All of these samples were previously collected and analyzed in Mahaney  
152 and Kalm (2000). Deane (2010) compared 9 Last Glacial Maximum (LGM) glaciogenic samples  
153 from Costa Rica with 9 potentially-glaciogenic samples from the Dominican Republic and found  
154 that the two sample sets were statistically indistinguishable, supporting a glaciogenic history for

**Table 2.** List of the samples from ancient depositional environments considered in this study. Each group of samples is assigned a number for reference in Figures 1, 2, and 6 (Column #). Column S indicates the number of samples in each sample group, and column N indicates the number of quartz grains in each sample group.

Study	#	Sample	Transport	S	N	GPS Point	Geologic Period
This Study	32	Brāvika Mbr. – Buldrevāgen (J1701-156)	Unknown	1	39	79°59'29"N, 17°31'20"E	Cryogenian
	33	Brāvika Mbr. – Buldrevāgen (J1701-166)	Unknown	1	40	79°59'29"N, 17°31'20"E	
Nartišs and Kalińska-Nartiša (2017)	34	Middle Gauja Lowland, Latvia (Mielupīte 1.3)	Aeolian	1	16	57°30'00"N, 26°00'00"E	Pleistocene
	35	Middle Gauja Lowland, Latvia (Mielupīte 1.7)	Aeolian	1	18	57°30'00"N, 26°00'00"E	
Deane (2010)	36	Till, Costa Rica (Sample 2)	Glacial	1	300	09°29'35"N, 83°29'07"W	Pleistocene
	37	Till, Costa Rica (Sample 3)	Glacial	1	100	09°29'35"N, 83°29'07"W	
	38	Till, Costa Rica (Sample 4)	Glacial	1	100	09°29'35"N, 83°29'07"W	
	39	Till, Costa Rica (Sample 5)	Glacial	1	100	09°29'35"N, 83°29'07"W	
	40	Till, Costa Rica (Sample 8)	Glacial	1	100	09°29'35"N, 83°29'07"W	
	41	Till, Dominican Republic (Sample 10)	Glacial	1	100	19°02'01"N, 71°04'22"W	
	42	Till, Dominican Republic (Sample 11)	Glacial	1	100	19°01'60"N, 71°04'26"W	
	43	Till, Dominican Republic (Sample 17)	Glacial	1	100	19°02'07"N, 71°04'38"W	
44	Till, Dominican Republic (Sample 18)	Glacial	1	100	19°01'39"N, 71°02'30"W		
Mahaney et al. (2001)	45	Arkūla Stage Sandstone, Estonia	Fluvial	21	420	58°15'00"N, 26°30'00"E	Middle Devonian
	46	Glaciofluvial Sand, Estonia	Fluvial	3	60	58°15'00"N, 26°30'00"E	Pleistocene
	47	Till, Estonia	Glacial	29	580	58°15'00"N, 26°30'00"E	
Mahaney and Kalm (1995)	48	Latvia Till, Estonia	Glacial	5	100	58°13'28"N, 26°25'16"E	Pleistocene
	49	Varduva Till, Estonia	Glacial	5	100	58°13'28"N, 26°25'16"E	
	50	Upper Ugandi Till, Estonia	Glacial	5	100	58°13'28"N, 26°25'16"E	
	51	Lower Ugandi Till, Estonia	Glacial	5	100	58°13'28"N, 26°25'16"E	
	52	Upper Dainava Till, Estonia	Glacial	3	60	58°13'28"N, 26°25'16"E	

155 the samples from the Dominican Republic. In our study, we include samples from Deane (2010)  
156 that were collected directly from known or hypothesized glacial diamicts and moraines in Costa  
157 Rica and the Dominican Republic; we did not include samples from glaciolacustrine  
158 environments and debris-flows. Nartišs and Kalińska-Nartiša (2017) analyzed two aeolian

159 samples from periglacial aeolian dunes associated with the retreat of the Fennoscandian ice sheet  
160 after the LGM in Latvia.

161

162

## METHODS

163

### *Field Work and Sample Collecting*

164 Samples analyzed for the first time in this study were collected over multiple field  
165 seasons using a variety of methods. The samples from the McMurdo Dry Valleys were originally  
166 collected as microbial mats using the methods described in Mackey et al. (2015), Jungblut et al.  
167 (2016), and Mackey et al. (2017). Samples from the Algodones Dunes and Waynoka Dunes were  
168 collected using the methods described in Adams and Soreghan (2020). On the Juneau Icefield,  
169 four sand samples of ~50 g each were collected in August 2019 from glacial moraines and an  
170 ephemeral glaciofluvial melt stream on the Llewellyn Glacier (Camp 26) nunatak. Field work on  
171 the Bråvika Member in Buldrevågen, Geerabukta, and Gimleodden was performed in 2017.

172

173

### *Microtextural Sample Disaggregation and SEM Preparation*

174 Most samples collected for this study were unconsolidated sediment, but consolidated  
175 samples were disaggregated before analysis. Both dolomite-cemented Bråvika Member samples  
176 from Svalbard were disaggregated using 1N hydrochloric acid (HCl) at 50°C for 24 hours. Sand  
177 samples from Lake Joyce, Lake Fryxell, and Lake Vanda were disaggregated from the microbial  
178 mats using 30% hydrogen peroxide (H<sub>2</sub>O<sub>2</sub>) solution at 50°C for 24 hours to remove organics and  
179 1N HCl at 50°C for 24 hours to remove carbonate.

180

181 All of the samples were then prepared for blind microtextural analysis in the style of  
Smith et al. (2018). Samples were distributed into vials and given unique codes unknown to the

182 primary researcher. These blinded conditions were maintained until after each sample's  
183 microtextural data were collected.

184 After sample randomization, each sample was gently wet sieved into a 125  $\mu\text{m}$  – 1 mm  
185 grain size fraction and dried in an oven. After drying, the samples were treated with 30%  $\text{H}_2\text{O}_2$   
186 solution at 50°C for 24 hours to remove organics. Samples were then treated with 1N HCl  
187 solution for 24 hours at 50°C to remove any remaining carbonate coatings. Neither  $\text{H}_2\text{O}_2$  nor  
188 low-concentration HCl at these temperatures and time frames affects quartz microtextures (Pye  
189 1983; Keiser et al. 2015; Smith et al. 2018).

190 Samples were then treated using the citrate-bicarbonate-dithionite (CBD) method  
191 (Janitsky 1986) to remove iron-oxide and manganese-oxide coatings. Between all chemical  
192 treatments, the samples were thoroughly rinsed and dried. These samples were not sonicated to  
193 prevent artificially inducing microtextures (Porter 1962).

194 Following these treatments, 50 grains that appeared to be quartz (e.g. translucent, no  
195 obvious cleavage, etc.) were randomly selected from each sample for microtextural analysis  
196 using a reflected-light microscope. The selected grains were mounted on an aluminum SEM stub  
197 with double-sided carbon tape in a 10x5 grid and then coated with a 5 nm thick platinum-  
198 palladium alloy (Pt/Pd; 80/20) sputter coating to prevent charging under the SEM. Although a  
199 gold (Au) or gold-palladium alloy (Au/Pd) coating is frequently used for SEM samples (Vos et  
200 al. 2014), Pt/Pd is a better alternative to Au coatings because Pt/Pd coatings have a smaller grain  
201 size that allows for higher-resolution analysis (5-10 nm Au vs. 4-8 nm Au/Pd vs. 2-3 nm Pt/Pd;  
202 Goldstein et al. 1992).

203

204

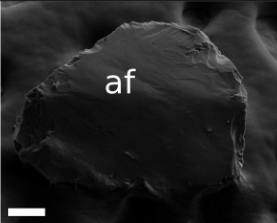
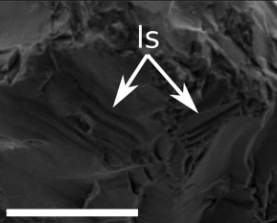
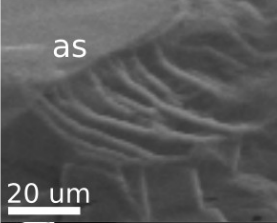
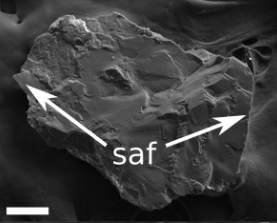
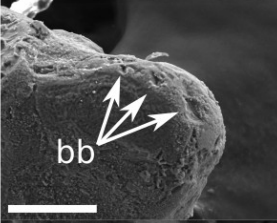
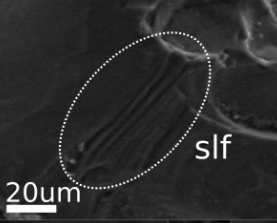
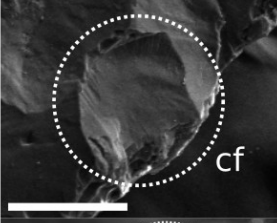
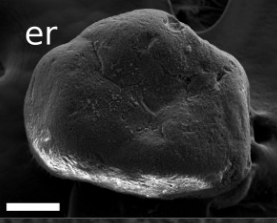
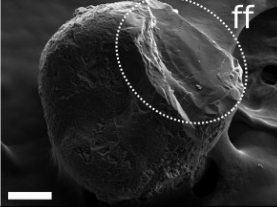
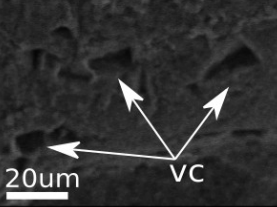
### *SEM Imaging and Analysis*

205 All grains in each sample were photographed at a 30° tilt on a Zeiss FESEM Supra55VP  
206 using a secondary electron (SE2) detector at 20 kV EHT. Viewing the grains at a 30° angle helps  
207 to identify smaller microtextures that are difficult to identify at a 0° angle (Margolis and Krinsley  
208 1971). During imaging, energy-dispersive spectroscopy (EDS) was used to confirm the  
209 composition of each quartz grain.

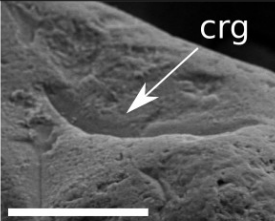
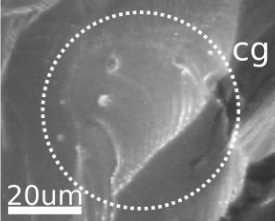
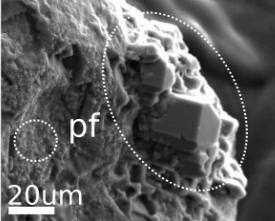
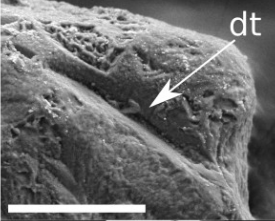
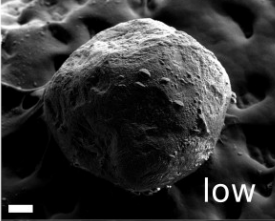
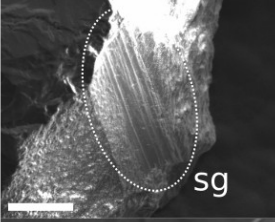
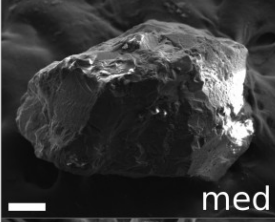
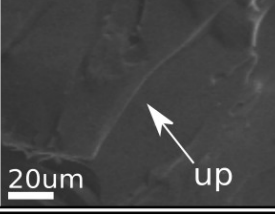
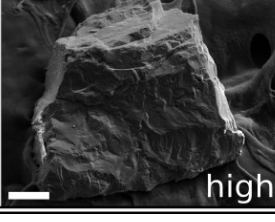
210 After imaging, each quartz grain was analyzed for the presence or absence of 20  
211 microtextures (Fig. 3) according to the methods of Mahaney et al. (2001) and Mahaney (2002).  
212 The microtextures are grouped into five bins as defined by Sweet and Soreghan (2010) that  
213 differentiate features by formation process: polygenetic, percussion, high-stress, chemical, and  
214 grain relief. The following formation descriptions are from Sweet and Soreghan (2010).  
215 Polygenetic features are formed through a variety of processes. Percussion features are formed  
216 via grain saltation. High-stress features are formed when grains are subjected to high shear  
217 stresses. Chemical features are formed via silica dissolution or precipitation. Grain relief refers to  
218 the difference between the high and low points on the grain surface.

219 Grains with extreme diagenetic overprint (e.g.  $\geq \sim 90\%$  estimated coverage of diagenetic  
220 overprint; Fig. S2) were removed from the sample dataset. The probability of occurrence for  
221 each microtexture  $p_m$  was calculated by dividing the sum of the counts for a given microtexture  
222 by the total number of grains in the sample (Smith et al. 2018).

223 Previous microtextural studies have used a range of sample sizes, from less than 20  
224 grains per sample (Krinsley and Funnell 1965; Coch and Krinsley 1971; Blackwelder and Pilkey  
225 1972) to 100 grains or more per sample (Vincent 1976; Setlow 1978; Deane 2010). This study  
226 analyzed  $\leq 50$  grains per sample as a midpoint between these. However, non-quartz grains and  
227 diagenetically overprinted grains were removed from the sample dataset, making 50 grains the

Microtexture	Abbr.	Description	Formation Process	Example Photo	Microtexture	Abbr.	Description	Formation Process	Example Photo
Abrasion Features	af	Rubbed or worn surface	Polygenetic		Linear Steps	ls	Widely spaced linear features, typically > 5 μm apart	Polygenetic	
Arc-Shaped Steps	as	Deep tears or breaks caused by impact; Several microns deep and typically spaced > 5 μm apart	Polygenetic		Sharp Angular Features	saf	Distinct sharp edges on grain surface	Polygenetic	
Breakage Blocks	bb	Blocky void marking removal of material, typically along an edge	Polygenetic		Subparallel Linear Fractures	slf	Linear fractures, typically < 5 μm spacing	Polygenetic	
Conchoidal Fractures	cf	Smooth, curved fracture	Polygenetic		Edge Rounding	er	Rounded edges on grains	Percussion	
Fracture Faces	ff	Smooth and clean fractures	Polygenetic		V-Shaped Percussion Cracks	vc	V-shaped fractures or indentions with typical sizes ranging from 1 μm to 30 μm	Percussion	

**Figure 3A.** Photos and description of microtextures used in this study. Scale bars are 100 μm unless otherwise noted.

Microtexture	Abbr.	Description	Formation Process	Example Photo	Microtexture	Abbr.	Description	Formation Process	Example Photo
Crescentic Gouges	crg	Crescent-shaped gouges with convex and concave limbs that have depths > 5 $\mu\text{m}$	High-Stress		Dissolution Etching	de	Cavities from chemical dissolution; often crystallographically oriented	Chemical	
Curved Grooves	cg	Curved abrasion feature caused by sustained high-stress contact with another grain, < 5 $\mu\text{m}$ deep	High-Stress		Precipitation Features	pf	Coatings of amorphous silica precipitation	Chemical	
Deep Troughs	dt	Grooves > 10 $\mu\text{m}$ deep	High-Stress		Low Relief	low	Nearly smooth surface without topographic irregularities	Entire history of grain	
Straight Grooves	sg	Linear grooves < 10 $\mu\text{m}$ deep	High-Stress		Medium Relief	med	Semi-smooth surface with topographic irregularities	Entire history of grain	
Upturned Plates	up	Surfaces of impact where plates of variable size are partially torn from surface, typically > 5 $\mu\text{m}$	High-Stress		High Relief	high	Topographically irregular surface with pronounced swells and swales	Entire history of grain	

**Figure 3B.** Photos and description of microtextures used in this study. Scale bars are 100  $\mu\text{m}$  unless otherwise noted.

228 upper limit for samples in this study. To address this, samples with  $\geq 15$  eligible quartz grains  
229 were considered statistically significant for analysis; samples with  $< 15$  eligible quartz grains  
230 were not analyzed. This limit of 15 grains was selected because it is the midpoint of the lower  
231 limit recommended sample sizes of Costa et al. (2012), who advocated for a median number of  
232 20 grains per sample, and of Vos et al. (2014), who advocated for a lower limit of 10 grains per  
233 sample.

234

### 235 *Principal Component Analysis (PCA)*

236 We performed PCA on the modern and ancient suites of microtextural data using Scikit-  
237 learn 0.21.2 (Pedregosa et al. 2011). This ordination excluded microtextures that were not  
238 analyzed by all authors, leaving 12 microtextures that were analyzed by every author in the  
239 dataset. These microtextures were arc-shaped steps, conchoidal fractures, linear steps, sharp  
240 angular features, subparallel linear fractures, edge rounding, v-shaped percussion cracks, curved  
241 grooves, precipitated features, low relief, medium relief, and high relief (Fig. 3; Tables S1–S2).

242 The principal component axes are first derived from the modern suite of microtextural  
243 data and then the ancient samples are fitted to these new axes. These axes are shown in three  
244 biplots: PC1 vs. PC2; PC1 vs. PC3; and PC2 vs. PC3. In each biplot, 95% confidence ellipses  
245 centered at the mean were calculated for each modern transport mode using the methods of  
246 Schelp (2019). The broken-stick criterion (Frontier 1976; Jackson 1993; Legendre and Legendre  
247 1998; Peres-Neto et al. 2003) was used to determine the significance of the microtextural  
248 loadings.

249

250

## **RESULTS**

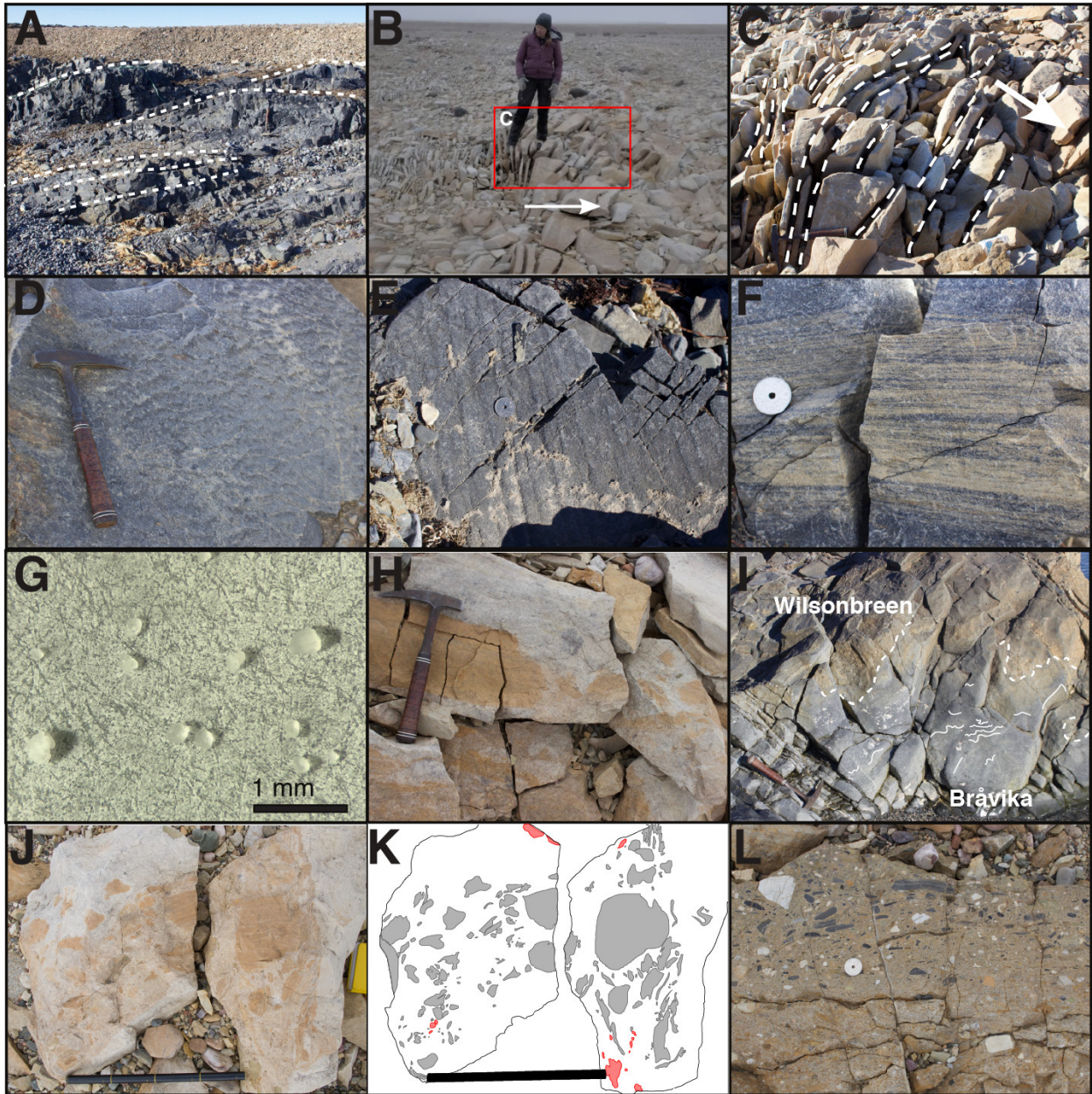


**Figure 4.** Field observations of the Bråvika Member and related units. All field photographs are of the Bråvika Member and are credited to K.D. Bergmann unless otherwise noted. A) Annotated photograph of large-scale bedforms exposed at Gimleodden. Dashed lines trace bedding surfaces. Hammer for scale. B) Photograph of frost-shattered trough crossbedding at 12 m in Buldrevågen (Fig. 2C), where the fracture planes are bedding surfaces. Arrow points upsection. The box highlights the location of C) (Photo credit: A.B. Jost). C) Annotated close-up of trough crossbedding. The dashed lines trace bedding surfaces and the arrow points upsection. D) Adherence ripples on a bedding plane at Geerabukta. E) Potential adherence ripples on a bedding plane at Gimleodden. F) Pinstripe lamination at Geerabukta. G) Photomicrograph of frosted grains from the Bråvika Member at Buldrevågen after dissolution of the dolomite cement with

acid (Photo credit: J.N. Reahl). H) Close-up of sand intraclasts with diffuse edges at Buldrevågen. I) Soft sediment deformation in the upper Bråvika Member under the Wilsonbreen tillite at Gimleodden, consistent with deformation of unlithified Bråvika sand by overriding ice. Dashed line marks the diffuse contact between the two units and solid lines trace contorted, folded beds within the Bråvika Member. Hammer for scale. J) Sandstone intraclasts with diffuse boundaries and greenish tan, pebbly, coarse sandstone intraclasts at 22 m in Buldrevågen (Fig. 2C). Bar is 40 cm long. K) Line drawing of J at the same scale; sandstone intraclasts are shaded gray, and greenish tan pebbly, coarse sandstone intraclasts are shaded red. L) The Wilsonbreen Formation at Buldrevågen, pictured here, has a greenish tan pebbly sandstone matrix.

251 *Bråvika Member Field Observations*

252 Field observations of the Bråvika Member in Buldrevågen (79°59'29"N, 17°31'20"E),  
253 Geerabukta (79°38'06"N, 17°43'48"E), and Gimleodden (79°48'19"N, 18°24'04"E) show  
254 evidence of bedforms with 5-10 m wavelength and 1-3 m amplitude, trough cross-bedding,  
255 adhesion ripples, pinstripe lamination (at 9 m in Fig. 2C) and grains that are frosted, well-  
256 rounded, and well-sorted (Fig. 4A-G). At the Gimleodden site, there is also evidence of soft  
257 sediment deformation in the Bråvika Member at the contact with the Wilsonbreen Formation  
258 (Fig. 4I). At the Buldrevågen site, the Bråvika Member hosts sandstone intraclasts with diffuse  
259 boundaries and no obvious cements at 22 m above the base of the Bråvika Member, as well as  
260 pebbly sandstone intraclast conglomerates at 18 m and 22 m (7 m and 3 m below the  
261 Wilsonbreen Formation contact, respectively; Figs. 2C, 4J-K). The pebbly sandstone intraclast  
262 conglomerate is similar in color to the overlying Wilsonbreen Formation (Fig. 4L).

263

264 *Microtextural Dataset Description*

265 This microtextural dataset is composed of 113 data points from modern and ancient  
266 aeolian, fluvial, and glacial settings. 92 of these data points come from modern settings and 21  
267 come from ancient settings. The data are compiled from 10 studies: this study (10% of the total



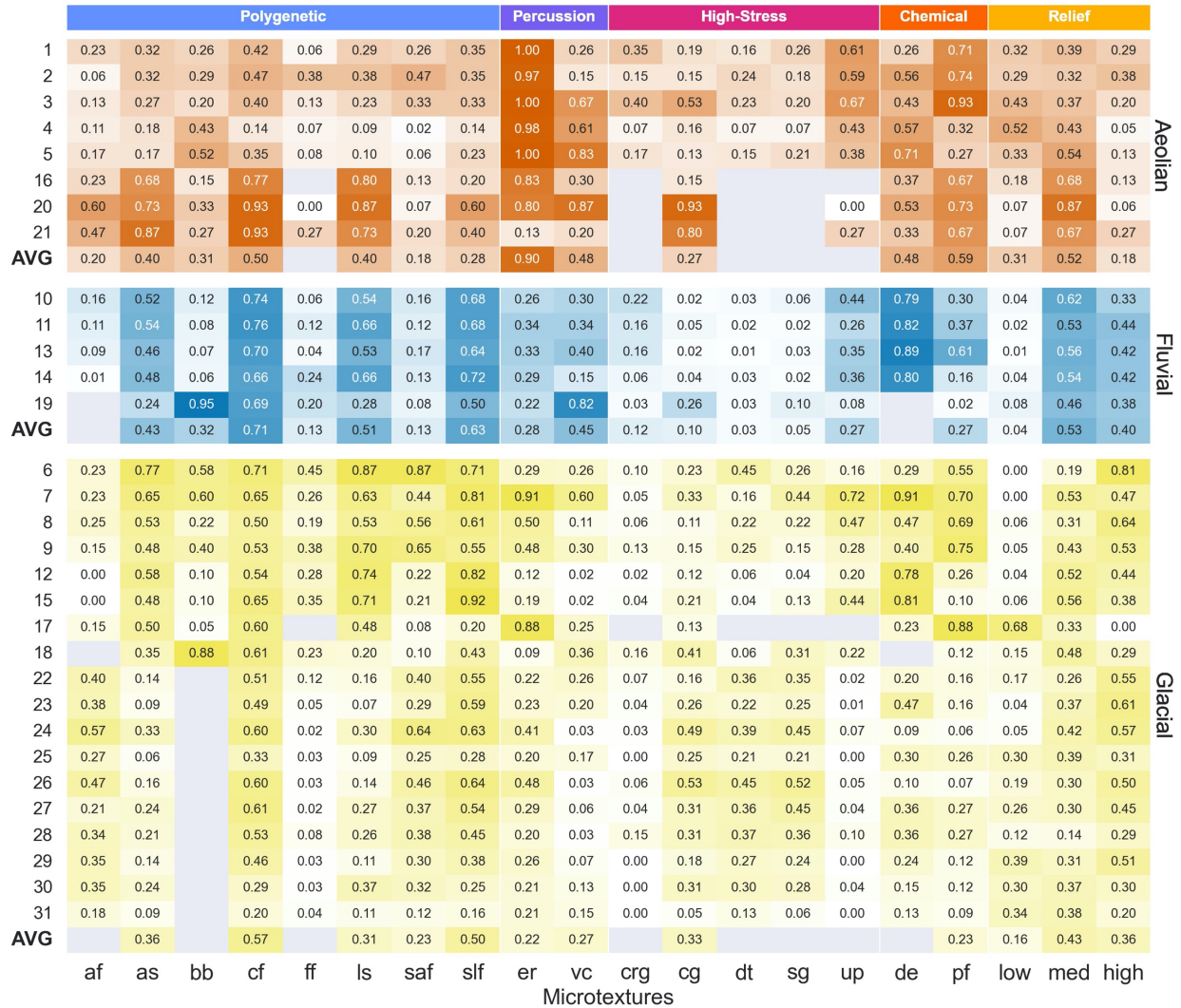


**Figure 5.** Heatmap of the microtextural probabilities of occurrence from 0 to 1 for each modern sample group used in the analysis. Samples are binned into aeolian, fluvial, and glacial transport modes. Refer to Table 1 for sample group numbers and descriptions. Data are averaged for sample groups that contain more than one sample ( $S > 1$ ). Refer to Figure 3A and B for microtextural abbreviations. The average of each transport mode for the modern samples (AVG) is at the bottom of each bin. Microtextures that were not analyzed within a study are grayed out.

291 glacial samples. The probability of occurrence of arc-shaped steps, conchoidal fractures, linear  
 292 steps, sharp angular features, and medium relief are not substantially different between the three  
 293 transport modes.

294 Study-specific variations in microtextural probabilities occur within each transport mode.  
295 In the aeolian transport mode, samples from Stevic (2015) (samples 20–21; Table 1) are more  
296 likely to have curved grooves (0.80–0.93) compared to other aeolian samples in the dataset  
297 (0.13–0.19). The fluvial grains from Sweet and Brannan (2016) (sample 19) are more likely to  
298 have v-shaped percussion cracks (0.82) compared to the remaining fluvial samples from Smith et  
299 al. (2018) (0.15–0.40). Glacial grains from this study (samples 6–9) and Kalińska-Nartiša et al.  
300 (2017) (sample 17) have the highest probabilities of edge rounding (0.29–0.91) and precipitated  
301 features (0.55–0.88) compared to the remaining glacial samples. The glacial grains from  
302 Kalińska-Nartiša et al. (2017) are also the most likely to have low relief (0.68).

303 **Ancient Samples.** — Both samples from the Cryogenian Brāvika Member (samples 32–  
304 33; Table 2) have high probabilities of edge rounding (1.00), precipitated features (1.00), and  
305 upturned plates (0.85–0.97; Fig. 6). Pleistocene aeolian sand samples from Nartišs and Kalińska-  
306 Nartiša (2017) (samples 34–35) have high abundances of edge rounding, dissolution etching, and  
307 precipitated features (all categorized as “abundant”; >0.75 probability of occurrence). Grains  
308 from the middle Devonian Arküla Stage fluvial sand samples (sample 45) and Pleistocene  
309 glaciofluvial sand samples (sample 46) from Estonia (Mahaney et al. 2001) are more likely to  
310 have edge rounding (0.56–0.64), v-shaped percussion cracks (0.53–0.61), and low relief (0.35–  
311 0.59) compared to grains from the modern fluvial average. The fluvial samples from Mahaney et  
312 al. (2001) also have lower probabilities of arc-shaped steps (0.00–0.23), conchoidal fractures  
313 (0.06–0.39), linear steps (0.00–0.26), subparallel linear fractures (0.08–0.35), upturned plates  
314 (0.00–0.04), and high relief (0.05–0.18) compared to the modern fluvial average. Grains from the  
315 Pleistocene tills in Costa Rica and the Dominican Republic (samples 36–44; Deane 2010) are  
316 more likely to have subparallel linear fractures (0.86–0.96) and medium relief (0.60–0.76)

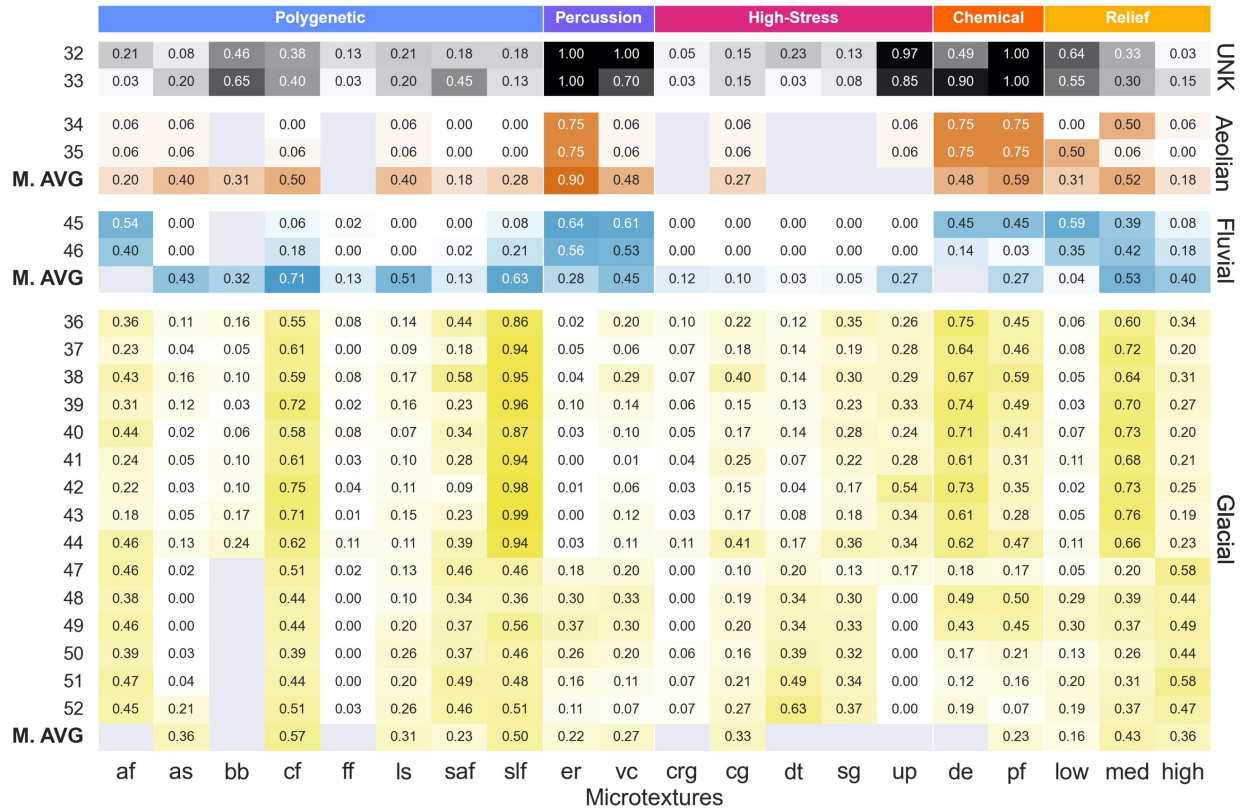


**Figure 6.** Heatmap of the microtextural probabilities of occurrence from 0 to 1 for each ancient sample group used in the analysis. Samples are binned into “unknown” (UNK; Bråvika Member), aeolian, fluvial, and glacial transport modes. Refer to Table 2 for sample group numbers and descriptions. Data are averaged for sample groups that contain more than one sample ( $S > 1$ ). Refer to Figure 3A and B for microtextural abbreviations. The average of each transport mode for the modern samples (M. AVG) from Figure 5 is at the bottom of each bin. Microtextures that were not analyzed within a study are grayed out.

317 compared to the modern glacial average. The Pleistocene tills from Mahaney et al. (2001)  
 318 (sample 47) and Mahaney and Kalm (1995) (samples 48-52) are broadly comparable to the  
 319 modern glacial average.

320

### 321 *Principal Component Analysis*

322 Within the PCA ordination, the PC1, PC2, and PC3 axes capture about 66% of the  
 323 variance in the modern dataset (27.01%, 21.33%, and 17.43%, respectively). Along the PC1 axis

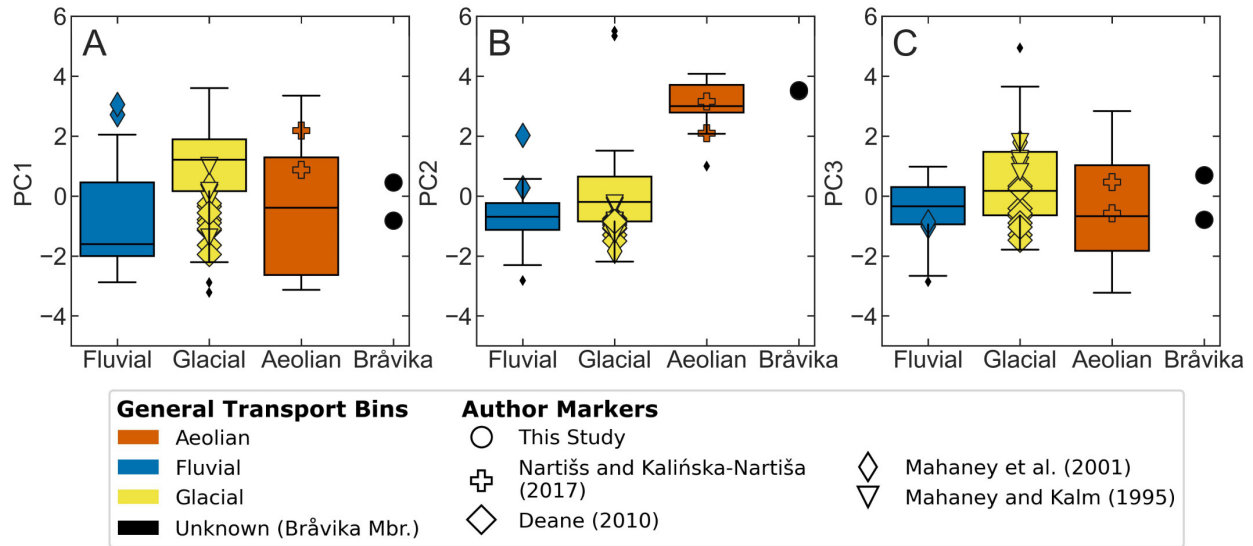


**Figure 7.** Boxplots of the modern aeolian, fluvial, and glacial samples along the PC1 (A), PC2 (B), and PC3 (C) axes. The small black diamonds represent modern outliers for each transport mode. The ancient samples are plotted as individual points over the boxplots.

324 (Figs. 7–8; Table S3), the aeolian, fluvial, and glacial samples are distributed along both sides of  
 325 the axis with no clear separation. However, the samples are generally separated by study along  
 326 PC1: the samples from Stevic (2015) and Smith et al. (2018) are distributed between -2.9 and -  
 327 1.1 and the samples from Mahaney et al. (1996) and Sweet and Brannan (2016) are distributed  
 328 between -0.2 and 3.5. The samples from this study and Kalińska-Nartiša et al. (2017) are widely  
 329 distributed on PC1, where the samples from this study are distributed between -3.2 to 3.3 and the  
 330 Kalińska-Nartiša et al. (2017) samples are distributed between -3.1 and 1.7. The sample  
 331 separation along PC1 is predominantly driven by the abundance of linear steps and arc-shaped  
 332 steps, which have the largest (-0.489) and second largest (-0.425) negative loadings along PC1  
 333 (Table 3). However, neither of these loadings are strongly associated with PC1 according to the  
 334 broken-stick criterion.

335 Along the PC2 axis, modern aeolian samples are distinctly separated from modern glacial  
 336 and fluvial samples. This separation between aeolian and fluvial/glacial samples along PC2 is

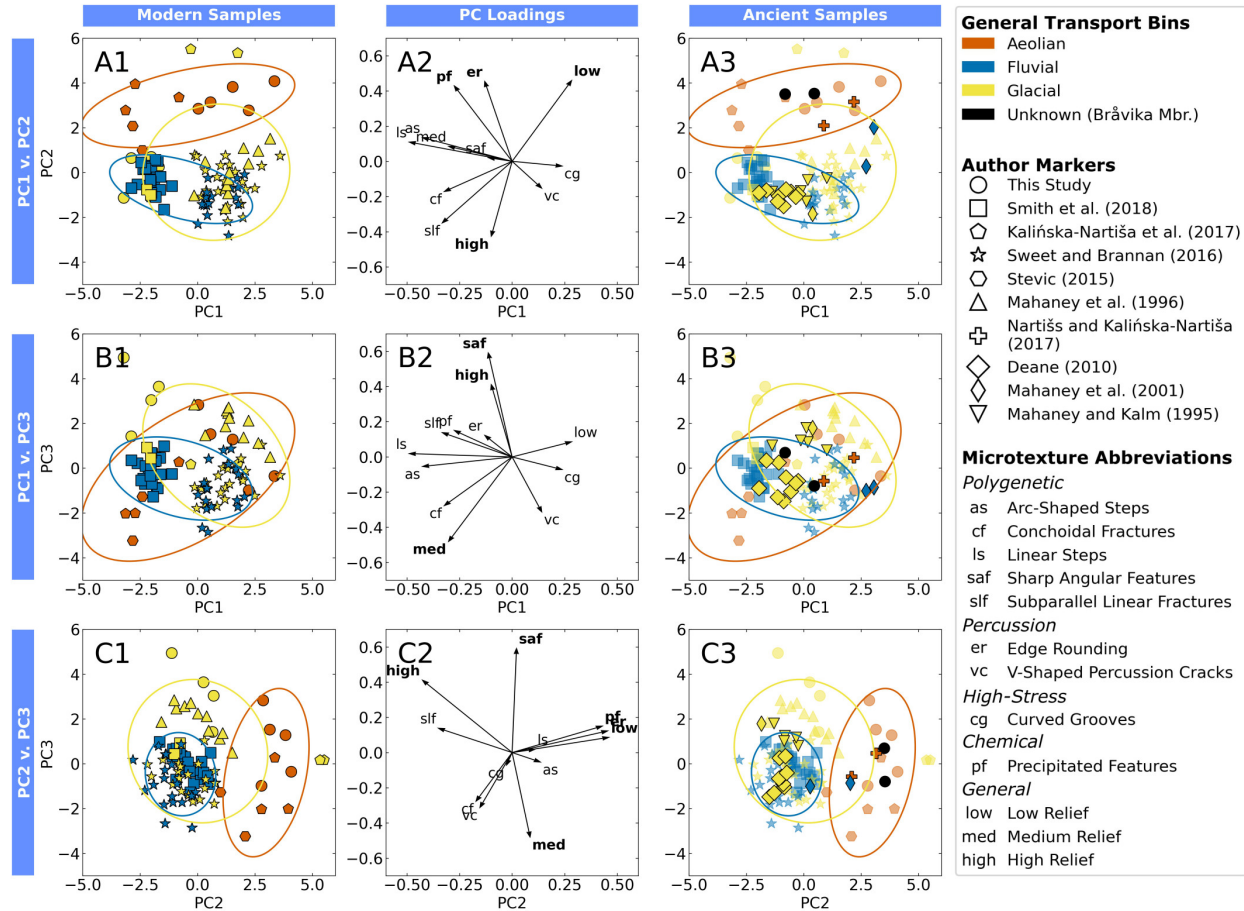


**Figure 8.** PCA ordination using all 12 microtextures analyzed by all studies. Each row is a biplot in A) PC1-PC2 space; B) PC1-PC3 space; and C) PC2-PC3 space. Column 1 plots the modern sample data within each space (this study through Mahaney et al. 1996), Column 2 plots the microtextural loadings, and Column 3 plots the ancient sample data (this study, Nartišs and Kalińska-Nartiša 2017 through Mahaney and Kalm 1995) over the existing modern reference frame. Refer to Table 3 for the loadings in Column 2. Microtextures with significant loadings in Column 2 are in bold. The ellipses are 95% confidence intervals of each modern transport mode that are centered at the mean of the transport mode in each coordinate space. The ellipses are calculated using the methods of Schelp (2019).

337 driven by low relief, edge rounding, and precipitated features in the positive direction (loadings  
 338 of 0.457, 0.455, and 0.432) and high relief in the negative direction (-0.427), which are all  
 339 associated with PC2 according to the broken-stick criterion.

340 Along the PC3 axis, the three transport modes are distributed along both sides of the axis  
 341 with no clear separation, similar to the distribution along PC1. However, unlike the distribution

**Table 3.** Ranked loadings and squared loadings of microtextures from the PCA ordination (Fig. 8). Refer to Figure 3A and B for microtexture abbreviations. The microtextures in bold have squared loadings that are greater than the expected value of their associated principal component according to the broken-stick criterion (Frontier 1976; Jackson 1993; Legendre and Legendre 1998; Peres-Neto et al. 2003).

PC1			PC2			PC3		
Expected PC Value:		0.259	Expected PC Value:		0.175	Expected PC Value:		0.134
Microtexture	Loading	Loading <sup>2</sup>	Microtexture	Loading	Loading <sup>2</sup>	Microtexture	Loading	Loading <sup>2</sup>
low	0.286	0.082	<b>low</b>	<b>0.457</b>	<b>0.209</b>	<b>saf</b>	<b>0.592</b>	<b>0.351</b>
cg	0.239	0.057	<b>er</b>	<b>0.455</b>	<b>0.207</b>	<b>high</b>	<b>0.411</b>	<b>0.169</b>
vc	0.141	0.020	<b>pf</b>	<b>0.432</b>	<b>0.186</b>	pf	0.153	0.023
high	-0.104	0.011	as	0.139	0.019	slf	0.135	0.018
saf	-0.114	0.013	ls	0.112	0.013	er	0.126	0.016
er	-0.128	0.017	med	0.090	0.008	low	0.089	0.008
pf	-0.272	0.074	saf	0.018	0.000	ls	0.019	0.000
med	-0.300	0.090	cg	-0.028	0.001	as	-0.055	0.003
cf	-0.324	0.105	vc	-0.153	0.023	cg	-0.071	0.005
slf	-0.335	0.112	cf	-0.168	0.028	cf	-0.279	0.078
as	-0.425	0.181	slf	-0.350	0.123	vc	-0.312	0.097
ls	-0.489	0.239	<b>high</b>	<b>-0.427</b>	<b>0.182</b>	<b>med</b>	<b>-0.482</b>	<b>0.232</b>

342 along PC1, the samples are not as distinctly separated by study. The significant microtextures  
 343 along PC3 are sharp angular features and high relief in the positive direction (0.592 and 0.411),  
 344 and medium relief in the negative direction (-0.482). All of these microtextures are associated  
 345 with PC3 according to the broken-stick criterion.

346 Along each principal component axis, at least 89% of the ancient aeolian, fluvial, and  
 347 glacial samples plot within the upper and lower adjacent values of the boxplot of their modern  
 348 counterparts: 89% on PC1, 95% on PC2, and 100% on PC3 (Fig. 7). In each biplot (Fig. 8), at  
 349 least 74% of these ancient samples plot within the 95% confidence ellipses of their modern  
 350 counterparts: 89% in the PC1-PC2 biplot (A3), 74% in the PC1-PC3 biplot (B3), and 95% in the  
 351 PC2-PC3 biplot (C3). The median of the percent agreement between the ancient samples and  
 352 their modern counterparts is 92%.

353           The 92% median agreement between the modern and ancient samples demonstrates that  
354 PCA of modern and ancient samples provides a valid framework for interpreting the fingerprint  
355 of depositional environments in ancient samples with ambiguous depositional histories. In this  
356 ordination, the two Bråvika Member samples with ambiguous depositional histories consistently  
357 plot within the upper and lower adjacent values of the modern aeolian samples in each principal  
358 component axis (Fig. 7) and the 95% confidence ellipses of the modern aeolian samples in each  
359 biplot (Fig. 8). This placement suggests that the Bråvika Member samples analyzed in this study  
360 have an aeolian origin.

361

362

## DISCUSSION

363

### *Interpreting the PCA Ordination*

364

365

366

367

368

369

370

371

372

373

374

375

PC1 separates the modern samples by author and accounts for the most variance in the dataset (27.01%), indicating that author-specific microtextural variance is the largest individual source of variance in the modern dataset. This result is consistent with the observation that SEM operator variance exerts significant influence on the probabilities of occurrence of individual microtextures (Culver et al. 1983). However, as Culver et al. (1983) observed using canonical variate analysis, author variance is overall negligible in determining a sample's depositional environment: the combined variance of PC2 and PC3 accounts for over a third of the variance in the modern dataset (21.33% and 17.43%, respectively). The PC2 axis separates the samples into aeolian and fluvial/glacial transport modes, and the PC3 axis separates the samples neither by transport mode nor by study (Fig. 8).

### *Which Microtextures Distinguish Transport Modes?*

376 Aeolian sediment is defined by high probabilities of low relief, edge rounding, and  
377 precipitated features, and fluvial and glacial sediments are defined by high probabilities of high  
378 relief and subparallel linear fractures. The modern (Fig. 5) and ancient (Fig. 6) heatmaps show  
379 that aeolian samples have the highest probabilities of low relief, edge rounding, and precipitated  
380 features, and fluvial and glacial samples have the highest probabilities of high relief and  
381 subparallel linear fractures. PC2 also separates the aeolian samples from the fluvial and glacial  
382 samples using low relief, edge rounding, and precipitated features in the positive (aeolian)  
383 direction and high relief in the negative (fluvial/glacial) direction (Fig. 8; Table 3). These  
384 findings are consistent with previous observations of these microtextures: low relief, edge  
385 rounding, and precipitated features have all previously been associated with windblown sediment  
386 (Nieter and Krinsley 1976; Lindé and Mycielska-Dowgiałło 1980; Krinsley and Trusty 1985;  
387 Mahaney 2002; Vos et al. 2014); high relief can occur on both fluvial and glacial sediments  
388 (Mahaney 2002; Vos et al. 2014); and subparallel linear fractures are often associated with  
389 glacial and glaciofluvial settings, the latter of which makes up 73% of the modern fluvial  
390 samples in this study (Mahaney and Kalm 2000; Deane 2010; Immonen 2013; Vos et al. 2014;  
391 Woronko 2016).

392 Although fluvial and glacial samples are microtexturally distinct from aeolian samples, it  
393 is difficult to disambiguate the fluvial and glacial transport modes from each other in this dataset.  
394 Features that are typically associated with glacial environments, such as arc-shaped steps,  
395 conchoidal fractures, linear steps, and sharp angular features (Mahaney and Kalm 2000;  
396 Mahaney 2002; Immonen 2013; Woronko 2016), had comparable probabilities across all three  
397 modern transport modes, indicating that these features are not exclusively associated with glacial  
398 environments (Fig. 5). Smith et al. (2018) also observed that arc-shaped steps and linear steps

399 may not be indicators of glacial transport. These results are consistent with Sweet and Soreghan  
400 (2010)'s classification of these features as *polygenetic* features that are formed through a variety  
401 of transport processes. Subparallel linear fractures are also associated with glacial and  
402 glaciofluvial settings (Mahaney and Kalm 2000; Deane 2010; Immonen 2013; Vos et al. 2014;  
403 Woronko 2016), but the modern fluvial average for subparallel linear fractures is higher than the  
404 glacial average. Although glaciofluvial samples make up 73% of the modern fluvial samples, the  
405 non-glacial fluvial samples (samples 10 and 13; Fig. 5) have similar probabilities of subparallel  
406 linear fractures compared to glaciofluvial samples (samples 11, 14, and 19), suggesting that  
407 subparallel linear fractures may not be an exclusively glacial feature. These results suggest that  
408 fluvial and glacial samples may share microtextural similarities, but more studies comparing the  
409 microtextural features of non-glacial fluvial, glaciofluvial, and glacial samples are needed to  
410 understand the differences between these transport environments.

411         These results highlight the importance of precipitated features as a primary indicator of  
412 transport instead of an exclusive product of diagenesis. If precipitated features were only an  
413 indicator of post-depositional diagenesis, then the probability of precipitated features should  
414 increase with age. However, all of the modern samples have some probability of having  
415 precipitated features—particularly the aeolian samples—and the ancient samples do not show a  
416 consistent increase in the probability of chemical features as the sediment age increases (Figs. 5–  
417 6). Both of these observations point to precipitated features being a primary microtextural  
418 feature. Although Sweet and Soreghan (2010) suggested that precipitated features should not be  
419 counted because they can form via diagenesis and overprint a sample, our results indicate that  
420 these features can also be a primary feature and should not be discounted, even in situations  
421 where diagenesis is a concern.



445 (Margolis and Krinsley 1971). Compared to the modern and ancient aeolian, fluvial, and glacial  
446 samples, the Bråvika Member samples are most similar to the aeolian samples, sharing similar  
447 probabilities of low relief, edge rounding, and precipitated features (Fig. 6). These samples also  
448 consistently plot within the upper and lower adjacent values (Fig. 7) and 95% confidence ellipse  
449 (Fig. 8) of the modern aeolian samples. Because the ancient aeolian, fluvial, and glacial samples  
450 are accurately matched with their modern counterparts 92% of the time when transformed into  
451 modern PCA space, the PCA ordination is able to accurately plot samples with ambiguous  
452 depositional histories alongside their most likely modern microtextural analogs.

453 An aeolian interpretation for the microtextural data is consistent with field observations  
454 made in 2017 of the Bråvika Member in Buldrevågen, Geerabukta, and Gimleodden (Fig. 4).  
455 Bedforms with 5–10 m wavelengths and 1–3 m amplitudes at the Gimleodden (Fig. 4A) and  
456 Buldrevågen (Fig. 4B–C) sites are consistent with aeolian dunes in scale and style (Wilson 1972;  
457 Pye and Tsoar 2009). There is also evidence of adhesion ripples on bedding planes at the  
458 Geerabukta (Fig. 4D) and Gimleodden (Fig. 4E) sites. Adhesion ripples are formed when dry,  
459 windblown sand is blown onto a wet surface, and these features have been previously observed  
460 on ancient aeolian deposits (Kocurek and Fielder 1982). The presence of pinstripe lamination at  
461 the Buldrevågen (Fig. 2C) and Geerabukta (Fig. 4F) sites are a strong indicator for aeolian  
462 deposition (Fryberger and Schenk 1988). The high degree of grain rounding at this interval (Fig.  
463 4G) is also characteristic of grains transported by aeolian processes (Folk 1980); subaqueous  
464 transport does not typically produce such a high degree of grain rounding (Pettijohn 1957). The  
465 frosted grains within these samples (Fig. 4G) are also a strong indicator of aeolian transport (Pye  
466 and Tsoar 2009).

467 Field evidence also suggests that the aeolian strata of the Bråvika Member may be syn-  
468 depositional with the Marinoan pan-glaciation as opposed to the Cryogenian interglacial. The  
469 pebbly sandstone intraclast conglomerates' proximity to the contact with—and similar color and  
470 texture as—the Wilsonbreen Formation (Figs. 2, 4) suggest that they are sourced from this unit.  
471 These intraclasts' occurrences at 7 m and 3 m below the Wilsonbreen Formation contact (Fig.  
472 2C) suggest that the Bråvika Member in Buldrevågen was syn-depositional with the Wilsonbreen  
473 Formation and the Marinoan pan-glaciation. The intraclasts with diffuse boundaries and no  
474 obvious cements at 22 m (Figs. 2, 4) are putative ice-cemented sand intraclasts. Ice-cemented  
475 intraclasts form when water within the pore space of unconsolidated sand freezes portions of  
476 sand into discrete clasts that can be transported and deformed into new orientations before the  
477 cementing ice melts. Sand intraclasts are routinely identified as ice-cemented in glaciogenic  
478 deposits (Browne and Naish 2003), and Runkel et al. (2010) has reported putative ice-cemented  
479 sand intraclasts preserved in rocks as old as the middle to late Cambrian. The putative ice-  
480 cemented intraclasts indicate that the Bråvika Member was at least unconsolidated during the  
481 Marinoan pan-glaciation, and the occurrence of possible Wilsonbreen intraclasts 3 m below the  
482 Wilsonbreen Formation contact (Fig. 2C) suggests that the upper Bråvika Member was syn-  
483 depositional with the Marinoan glaciation. Evidence of soft sediment deformation at the contact  
484 between the Bråvika Member and Wilsonbreen Formation at Gimleodden (Fig. 4I) is also  
485 consistent with the upper Bråvika Member being unconsolidated during the Marinoan glaciation.

486 Integrating microtextural and field observations, we suggest that the upper Bråvika  
487 Member includes aeolian deposition and may represent a syn-glacial aeolian sand sea, or erg,  
488 contemporaneous with the Marinoan glaciation. This setting is akin to previously identified  
489 Marinoan syn-glacial ergs in the Bakoye Formation of Mali (Deynoux et al. 1989) and the

490 Whyalla Sandstone (Elatina glaciation) of South Australia (Williams 1998; Rose et al. 2013;  
491 Ewing et al. 2014). Hoffman and Li (2009) suggested that katabatic winds coming off of the  
492 Marinoan ice sheet are the primary transport mechanism for these syn-glacial ergs. The  
493 northward paleoflow direction of the Bråvika Member and the Bråvika Member's reciprocal  
494 thickness relationship with the Wilsonbreen Formation (Halverson et al. 2004) may reflect this  
495 transport mechanism, where a northward-advancing ice margin represented by the Wilsonbreen  
496 Formation drives the Bråvika Member to the north with katabatic winds coming off of the  
497 Marinoan ice sheet.

498         The microtextural samples analyzed in this study are specific to the interval in  
499 Buldrevågen that is proximal to the Wilsonbreen contact. Given the wide range of possible facies  
500 proposed by Halverson et al. (2004), Halverson (2011), Hoffman et al. (2012), and this study, the  
501 Bråvika Member may represent multiple depositional environments across localities that capture  
502 a transition from the Cryogenian interglacial to the Marinoan pan-glaciation.

503         Important questions remain about the apportionment of time within the strata that record  
504 the Cryogenian interglacial in Svalbard. The absence of the pre-Marinoan Trezona negative  $\delta^{13}\text{C}$   
505 excursion below the Wilsonbreen Formation has been used to suggest that the sedimentary  
506 package between the Petrovbreen Member and the Wilsonbreen Formation is top-truncated  
507 (Hoffman et al. 2012; Fairchild et al. 2016; Halverson et al. 2018). The locations of the hiatal  
508 surfaces within the Bråvika Member remain ambiguous, and their locations are critical to  
509 understanding the apportionment of time in these units and in the interglacial. Our work suggests  
510 that the uppermost aeolian deposition within the Bråvika Member is continuous with the start of  
511 Wilsonbreen deposition, but there may be important hiatal surfaces lower in the Bråvika  
512 Member.

513

514

## CONCLUSIONS

515

516

517

518

519

520

521

522

523

524

525

526

527

528

529

530

531

532

533

534

535

Quartz surface microtextures preserve the transport histories of modern and ancient sediment. However, because workers count microtextures differently for samples from the same depositional environment, the defining microtextures of certain transport modes are not well constrained. We used PCA to directly compare quantitative microtextural data from modern and ancient aeolian, fluvial, and glacial sediments across workers. Although differences between workers are the largest sources of variance in the dataset, the PCA ordination shows that aeolian samples are microtexturally distinct from fluvial and glacial samples across studies. Fluvial and glacial samples are difficult to disambiguate from each other in this dataset, indicating that more work needs to be done comparing fluvial, glaciofluvial, and glacial samples with each other. The PCA ordination also demonstrates that ancient sediments and modern sediments have quantitatively similar microtextural relationships. Therefore, PCA may be a useful tool to elucidate the ambiguous transport histories of some ancient sediment grains. As a test case, we used PCA to constrain the depositional environment of the ambiguous Cryogenian Bråvika Member from Svalbard. This ordination, combined with field observations, indicates that the Bråvika Member includes aeolian deposition, and suggests that the Bråvika Member may be analogous to syn-glacial Marinoan aeolian sand seas such as the Bakoye Formation in Mali and the Whyalla Sandstone in South Australia. This study demonstrates that PCA can distinguish sedimentary environments across multiple studies, which in turn helps constrain the depositional history of ambiguous sedimentary deposits like the Bråvika Member.

## SUPPLEMENTARY MATERIAL

536 All supplementary materials related to this study—including detailed sample  
537 descriptions, additional notes on PCA analysis, code, raw microtextural data, and SEM images—  
538 are available at [https://github.com/jreahl/Reahl\\_2020](https://github.com/jreahl/Reahl_2020).

539

540

#### LAND ACKNOWLEDGEMENT

541 This work—from analysis to writing—was performed at institutions built on Indigenous  
542 land, using samples collected from Indigenous lands. The samples analyzed for the first time in  
543 this study were collected from the traditional and ancestral territories of the Cocopah (*Kwapa*),  
544 Comanche (*Numunuu*), Keechi (*Ki:che:ss*), Kiowa (*[Gáui[dòñ:gyà]*), Kumeyaay, Osage  
545 (*Wahzhazhe*), Quechan (*Kwatsáan*), Salt River O’odham (Pima) and Piipaash (Maricopa), Taku  
546 River Tlingit (*Lingít*), Tawakoni (*Tawá:kharih*), Waco (*Wi:ko?*), and Wichita (*Kirikir?i:s*).  
547 Laboratory analysis and SEM analysis was performed on unceded Wampanoag land. Writing  
548 was performed on the territories of the Abenaki, Chumash, and Wampanoag. These communities  
549 occupied these territories before and after European colonization and live on this land to the  
550 present day. We also acknowledge the dispossession of Indigenous land through the 1862 Morrill  
551 Act, which turned parcels of land taken from tribal nations into seed money for land-grant  
552 universities including the Massachusetts Institute of Technology. Although this  
553 acknowledgement does not compensate for centuries of injustices, we hope it helps spur robust,  
554 mutually beneficial collaboration between Indigenous communities and scientific efforts. We  
555 encourage readers to engage with Indigenous communities and cultures around where they live  
556 and work. The Native Land Digital database ([native-land.ca](http://native-land.ca)) is an excellent resource to begin  
557 this process. The best resources for prolonged learning are through direct conversation and  
558 collaboration with Indigenous community members. Many Indigenous communities have

559 dedicated cultural heritage officers who may be available as partners in these efforts; the  
560 National Congress of American Indians (ncai.org) hosts a tribal directory with contact  
561 information, as well as the National Association of Tribal Historic Preservation Officers  
562 (nathpo.org).

563

## 564 **ACKNOWLEDGEMENTS**

565 We thank the Salt River Pima-Maricopa Indian Community Cultural Resource  
566 Department, Justin Brundin (Cultural Resources Manager, Cocopah Indian Tribe), Andrea A.  
567 Hunter (Tribal Historic Preservation Officer, Osage Nation), Gary McAdams (Cultural Planner,  
568 Wichita and Affiliated Tribes), and Benjamin Louter (Heritage Coordinator, Taku River Tlingit  
569 First Nation) for assistance with acknowledging Indigenous territory. Adam B. Jost  
570 (Massachusetts Institute of Technology) performed field work in Svalbard with M.D.C., J.W.,  
571 T.J.M., and K.D.B.; collected photographs; and trained and assisted J.N.R. in the laboratory. We  
572 thank Steven M. Adams and Gerilyn S. Soreghan (University of Oklahoma) for collecting and  
573 providing samples from the Algodones Dunes and the Waynoka Dunes. The Juneau Icefield  
574 Research Program (JIRP), Foundation for Glacier and Environmental Research (FGER), and  
575 Coastal Helicopters in Juneau, Alaska provided logistical support, food, and lodging on the  
576 Juneau Icefield. This work began as J.N.R.'s undergraduate thesis project at Wellesley College.  
577 We thank Daniel J. Brabander, Katrin Monecke, and Wesley A. Watters at Wellesley College for  
578 being on the thesis committee. We thank Timothy J. Cavanaugh at the Harvard University Center  
579 for Nanoscale Systems (CNS) for assistance operating the SEM. The Harvard CNS is a member  
580 of the National Nanotechnology Coordinated Infrastructure Network (NNCI), which is supported  
581 by the National Science Foundation under NSF award no. 1541959. K.D.B. acknowledges

582 support from the Victor P. Starr Development Chair and the David and Lucille Packard  
583 Foundation. M.D.C. received support from a National Defense Science and Engineering  
584 Graduate Fellowship. J.W. received support from the Dean of the School of Science Fellowship  
585 at MIT. T.J.M. received support from the Agouron Geobiology Institute. Field work in Svalbard  
586 was supported by the MIT Wade Fund awarded to K.D.B. Field work on the Juneau Icefield was  
587 partially funded by the National Association of Geoscience Teachers (NAGT) Scholarship for  
588 Field Study awarded to J.N.R. Thoughtful feedback from Pedro J.M. Costa and an anonymous  
589 reviewer improved the manuscript.

590

591

#### **AUTHOR CONTRIBUTIONS**

592 J.N.R. wrote the manuscript, collected samples from the Juneau Icefield, performed SEM  
593 analysis on all samples, and performed the PCA analysis. M.D.C. and K.D.B. were the primary  
594 advisors to J.N.R. J.W. shared her stratigraphic columns and samples of the Bråvika Member, as  
595 well as insight on statistics and machine learning. J.W., M.D.C., T.J.M., and K.D.B.  
596 characterized and collected samples of the Bråvika Member in Svalbard during their 2017 field  
597 season. T.J.M. contributed samples from the McMurdo Dry Valleys. All authors reviewed the  
598 final manuscript.

599

600

#### **REFERENCES**

- 601 Adams, S. M., 2018, Evaluating desert silt production using field, experimental, and remote-  
602 sensing methods [MS Thesis]: University of Oklahoma, 74 p.
- 603 Adams, S. M., and Soreghan, G. S., 2020, A test of the efficacy of sand saltation for silt  
604 production: Implications for the interpretation of loess: *Geology*, v. 48, p. 1105–1109.
- 605 Blackwelder, P. L., and Pilkey, O. H., 1972, Electron microscopy of quartz grain surface  
606 textures: the U.S. Eastern Atlantic continental margin: *Journal of Sedimentary Petrology*,  
607 v. 42, p. 520–526.

- 608 Browne, G. H., and Naish, T. R., 2003, Facies development and sequence architecture of a late  
609 Quaternary fluvial-marine transition, Canterbury Plains and shelf, New Zealand:  
610 implications for forced regressive deposits: *Sedimentary Geology*, v. 158, p. 57–86.
- 611 Bull, P. A., 1981, Environmental reconstruction by electron microscopy: *Progress in Physical*  
612 *Geography*, v. 5, p. 368–397.
- 613 Calver, C. R., Crowley, J. L., Wingate, M. T. D., Evans, D. A. D., Raub, T. D., and Schmitz, M.  
614 D., 2013, Globally synchronous Marinoan deglaciation indicated by U-Pb geochronology  
615 of the Cottons Breccia, Tasmania, Australia: *Geology*, v. 41, p. 1127–1130.
- 616 Coch, N. K., and Krinsley, D. H., 1971, Comparison of stratigraphic and electron microscopic  
617 studies in Virginia Pleistocene coastal sediments: *The Journal of Geology*, v. 79, p. 426–  
618 437.
- 619 Condon, D., Zhu, M., Bowring, S., Wang, W., Yang, A., and Jin, Y., 2005, U-Pb Ages from the  
620 Neoproterozoic Doushantuo Formation, China: *Science*, v. 308, p. 95–98.
- 621 Costa, P. J. M., Andrade, C., Dawson, A. G., Mahaney, W. C., Freitas, M. C., Paris, R., and  
622 Taborda, R., 2012, Microtextural characteristics of quartz grains transported and  
623 deposited by tsunamis and storms: *Sedimentary Geology*, v. 275–276, p. 55–69.
- 624 Costa, P. J. M., Andrade, C., Mahaney, W. C., Marques da Silva, F., Freire, P., Freitas, M. C.,  
625 Janardo, C., Oliveira, M. A., Silva, T., and Lopes, V., 2013, Aeolian microtextures in  
626 silica spheres induced in a wind tunnel experiment: Comparison with aeolian quartz:  
627 *Geomorphology*, v. 180–181, p. 120–129.
- 628 Costa, P. J. M., Park, Y. S., Kim, Y. D., Quintela, M., Mahaney, W. C., Dourado, F., and  
629 Dawson, S., 2017, Imprints In Silica Grains Induced During An Open-Channel Flow  
630 Experiment: Determination of Microtextural Signatures During Aqueous Transport:  
631 *Journal of Sedimentary Research*, v. 87, p. 677–687.
- 632 Culver, S. J., Bull, P. A., Campbell, S., Shakesby, R. A., and Whalley, W. B., 1983,  
633 Environmental discrimination based on quartz grain surface textures: a statistical  
634 investigation: *Sedimentology*, v. 30, p. 129–136.
- 635 Deane, S. M., 2010, Quartz grain microtextures and sediment provenance: Using scanning  
636 electron microscopy to characterize tropical highland sediments from Costa Rica and the  
637 Dominican Republic [MS Thesis]: University of Tennessee, Knoxville, 137 p.
- 638 Deynoux, M., Kocurek, G., and Proust, J. N., 1989, Late Proterozoic periglacial aeolian deposits  
639 on the West African Platform, Taoudeni Basin, western Mali: *Sedimentology*, v. 36, p.  
640 531–549.
- 641 Ewing, R. C., Eisenman, I., Lamb, M. P., Poppick, L., Maloof, A. C., and Fischer, W. W., 2014,  
642 New constraints on equatorial temperatures during a Late Neoproterozoic snowball Earth  
643 glaciation: *Earth and Planetary Science Letters*, v. 406, p. 110–122.

- 644 Fairchild, I. J., Fleming, E. J., Bao, H., Benn, D. I., Boomer, I., Dublyansky, Y. V., Halverson,  
645 G. P., Hambrey, M. J., Hendy, C., McMillan, E. A., Spötl, C., Stevenson, C. T. E., and  
646 Wynn, P. M., 2016, Continental carbonate facies of a Neoproterozoic panglaciation,  
647 north-east Svalbard (G. Spence, Ed.): *Sedimentology*, v. 63, p. 443–497.
- 648 Folk, R. L., 1980, *Petrology of Sedimentary Rocks*: Hemphill Publishing Company.
- 649 Frontier, S., 1976, Étude de la décroissance des valeurs propres dans une analyse en composantes  
650 principales: comparaison avec le modèle du bâton brisé: *Journal of Experimental Marine*  
651 *Biology*, v. 25, p. 67–75.
- 652 Fryberger, S. G., and Schenk, C. J., 1988, Pin stripe lamination: a distinctive feature of modern  
653 and ancient eolian sediments: *Sedimentary Geology*, v. 55, p. 1–15.
- 654 Goldstein, J. I., Newbury, D. E., Echlin, P., Joy, D. C., Romig Jr., A. D., Lyman, C. D., Fiori, C.,  
655 and Lifshin, E., 1992, *Scanning Electron Microscopy and X-Ray Microanalysis*:  
656 Springer.
- 657 Green, W. J., Stage, B. R., Bratina, B. J., Wagers, S., Preston, A., O’Bryan, K., Shacat, J., and  
658 Newell, S., 2004, Nickel, Copper, Zinc and Cadmium Cycling with Manganese in Lake  
659 Vanda (Wright Valley, Antarctica): *Aquatic Geochemistry*, v. 10, p. 303–323.
- 660 Gumbley, J. W., 1975, A sedimentological study of three saline lakes in the Dry Valleys of  
661 Victoria Land, Antarctica [MS Thesis]: University of Waikato, 165 p.
- 662 Halverson, G. P., Maloof, A. C., and Hoffman, P. F., 2004, The Marinoan glaciation  
663 (Neoproterozoic) in northeast Svalbard: *Basin Research*, v. 16, p. 297–324.
- 664 Halverson, G. P., 2011, Chapter 55 Glacial sediments and associated strata of the Polarisbreen  
665 Group, northeastern Svalbard: *Geological Society, London, Memoirs*, v. 36, p. 571–579.
- 666 Halverson, G. P., Kunzmann, M., Strauss, J. V., and Maloof, A. C., 2018, The Tonian-  
667 Cryogenian transition in Northeastern Svalbard: *Precambrian Research*, v. 319, p. 79–95.
- 668 Hoffman, P. F., and Li, Z.-X., 2009, A palaeogeographic context for Neoproterozoic glaciation:  
669 *Palaeogeography, Palaeoclimatology, Palaeoecology*, v. 277, p. 158–172.
- 670 Hoffman, P. F., Halverson, G. P., Domack, E. W., Maloof, A. C., Swanson-Hysell, N. L., and  
671 Cox, G. M., 2012, Cryogenian glaciations on the southern tropical paleomargin of  
672 Laurentia (NE Svalbard and East Greenland), and a primary origin for the upper Russøya  
673 (Islay) carbon isotope excursion: *Precambrian Research*, v. 206–207, p. 137–158.
- 674 Immonen, N., 2013, Surface microtextures of ice-rafted quartz grains revealing glacial ice in the  
675 Cenozoic Arctic: *Palaeogeography, Palaeoclimatology, Palaeoecology*, v. 374, p. 293–  
676 302.
- 677 Jackson, D. A., 1993, Stopping rules in principal components analysis: a comparison of  
678 heuristical and statistical approaches: *Ecology*, v. 74, p. 2204–2214.

- 679 Janitsky, P., 1986, Laboratory methods: Citrate-bicarbonate-dithionite (CBD) extractable iron  
680 and aluminum, *in* Field and laboratory procedures used in a soil chronosequence study:,  
681 p. 38–41.
- 682 Jungblut, A. D., Hawes, I., Mackey, T. J., Krusor, M., Doran, P. T., Sumner, D. Y., Eisen, J. A.,  
683 Hillman, C., and Goroncy, A. K., 2016, Microbial Mat Communities along an Oxygen  
684 Gradient in a Perennially Ice-Covered Antarctic Lake (A. J. Stams, Ed.): *Applied and  
685 Environmental Microbiology*, v. 82, p. 620–630.
- 686 Kalińska-Nartiša, E., Lamsters, K., Karušs, J., Krievāns, M., Rečs, A., and Meija, R., 2017,  
687 Quartz grain features in modern glacial and proglacial environments: A microscopic  
688 study from the Russell Glacier, southwest Greenland: *Polish Polar Research*, v. 38, p.  
689 265–289.
- 690 Keiser, L. J., Soreghan, G. S., and Kowalewski, M., 2015, Use of Quartz Microtextural Analysis  
691 To Assess Possible Proglacial Deposition For the Pennsylvanian–Permian Cutler  
692 Formation (Colorado, U.S.A.): *Journal of Sedimentary Research*, v. 85, p. 1310–1322.
- 693 Kendall, B., Creaser, R. A., and Selby, D., 2006, Re-Os geochronology of postglacial black  
694 shales in Australia: Constraints on the timing of “Sturtian” glaciation: *Geology*, v. 34, p.  
695 729.
- 696 Kocurek, G., and Fielder, G., 1982, Adhesion structures: *Journal of Sedimentary Petrology*, v.  
697 52, p. 1229–1241.
- 698 Krinsley, D., and Takahashi, T., 1962, Applications of electron microscopy to geology, *in*  
699 *Transactions of the New York Academy of Sciences*, p. 3–22.
- 700 Krinsley, D. H., and Funnell, B. M., 1965, Environmental history of quartz sand grains from the  
701 Lower and Middle Pleistocene of Norfolk, England: *Quarterly Journal of the Geological  
702 Society of London*, v. 121, p. 435–456.
- 703 Krinsley, D., and Doornkamp, J. C., 1973, *Atlas of Sand Grain Surface Textures*: Cambridge  
704 University Press.
- 705 Krinsley, D. H., and Trusty, P., 1985, Environmental interpretation of quartz grain surface  
706 textures, *in* *Provenance of Arenites*: Springer.
- 707 Křížek, M., Krbcová, K., Mida, P., and Hanáček, M., 2017, Micromorphological changes as an  
708 indicator of the transition from glacial to glaciofluvial quartz grains: Evidence from  
709 Svalbard: *Sedimentary Geology*, v. 358, p. 35–43.
- 710 Legendre, P., and Legendre, L., 1998, *Numerical ecology*: Elsevier Science BV.
- 711 Lepper, K., and Scott, G. F., 2005, Late Holocene aeolian activity in the Cimarron River valley  
712 of west–central Oklahoma: *Geomorphology*, v. 70, p. 42–52.

- 713 Lindé, K., and Mycielska-Dowgiałło, E., 1980, Some experimentally produced microtextures on  
714 grain surfaces of quartz sand: *Geografiska Annaler*, v. 62, p. 171–184.
- 715 Mackey, T. J., Sumner, D. Y., Hawes, I., Jungblut, A. D., and Andersen, D. T., 2015, Growth of  
716 modern branched columnar stromatolites in Lake Joyce, Antarctica: *Geobiology*, v. 13, p.  
717 373–390.
- 718 Mackey, T. J., Sumner, D. Y., Hawes, I., and Jungblut, A. D., 2017, Morphological signatures of  
719 microbial activity across sediment and light microenvironments of Lake Vanda,  
720 Antarctica: *Sedimentary Geology*, v. 361, p. 82–92.
- 721 Mahaney, W. C., and Kalm, V., 1995, Scanning electron microscopy of Pleistocene tills in  
722 Estonia: *Boreas*, v. 24, p. 13–29.
- 723 Mahaney, W. C., Claridge, G., and Campbell, I., 1996, Microtextures on quartz grains in tills  
724 from Antarctica: *Palaeogeography, Palaeoclimatology, Palaeoecology*, v. 121, p. 89–103.
- 725 Mahaney, W. C., and Kalm, V., 2000, Comparative scanning electron microscopy study of  
726 oriented till blocks, glacial grains and Devonian sands in Estonia and Latvia: *Boreas*, v.  
727 29, p. 35–51.
- 728 Mahaney, W. C., Stewart, A., and Volli, K., 2001, Quantification of SEM microtextures useful in  
729 sedimentary environmental discrimination: *Boreas*, v. 30, p. 165–171.
- 730 Mahaney, W. C., 2002, *Atlas of Sand Grain Surface Textures and Applications*: Oxford  
731 University Press.
- 732 Margolis, S. V., and Krinsley, D. H., 1971, Submicroscopic frosting on eolian and subaqueous  
733 quartz sand grains: *Geological Society of America Bulletin*, v. 82, p. 3395–3406.
- 734 Margolis, S. V., and Krinsley, D. H., 1974, Processes of formation and environmental occurrence  
735 of microfeatures on detrital quartz grains: *American Journal of Science*, v. 274, p. 449–  
736 464.
- 737 Nartišs, M., and Kalińska-Nartiša, E., 2017, An aeolian or a glaciolacustrine record? A case  
738 study from Mielūpīte, Middle Gauja Lowland, northeast Latvia: *Geologos*, v. 23, p. 15–  
739 28.
- 740 Nieter, W. M., and Krinsley, D. H., 1976, The production and recognition of aeolian features on  
741 sand grains by silt abrasion: *Sedimentology*, v. 23, p. 713–720.
- 742 Pedregosa, F., Varoquaux, G., Gramfort, A., Michel, V., Thirion, B., Grisel, O., Blondel, M.,  
743 Prettenhofer, P., Weiss, R., Dubourg, V., Vanderplas, J., Passos, A., Cournapeau, D.,  
744 Brucher, M., and others, 2011, Scikit-learn: Machine Learning in Python: *Journal of*  
745 *Machine Learning Research*, v. 12, p. 2825–2830.

- 746 Peres-Neto, P. R., Jackson, D. A., and Somers, K. M., 2003, Giving meaningful interpretation to  
747 ordination axes: assessing loading significance in principal component analysis: *Ecology*,  
748 v. 84, p. 2347–2363.
- 749 Pettijohn, F. J., 1957, Paleocurrents of Lake Superior Precambrian quartzites: *Bulletin of the*  
750 *Geological Society of America*, v. 68, p. 469–480.
- 751 Pippin, M., 2016, Progressive downstream overprinting of glacially induced quartz microtextures  
752 during fluvial saltation, Salmon River, British Columbia and Alaska [MS Thesis]: Texas  
753 Tech University, 85 p.
- 754 Porter, J. J., 1962, Electron microscopy of sand surface texture: *Journal of Sedimentary*  
755 *Petrology*, v. 32, p. 124–135.
- 756 Prave, A. R., Condon, D. J., Hoffmann, K. H., Tapster, S., and Fallick, A. E., 2016, Duration and  
757 nature of the end-Cryogenian (Marinoan) glaciation: *Geology*, v. 44, p. 631–634.
- 758 Pye, K., 1983, Coastal Dunes: *Progress in Physical Geography*, v. 7, p. 531–557.
- 759 Pye, K., and Tsoar, H., 2009, *Aeolian sand and sand dunes*: Springer, 458 p.
- 760 Říha, K., Křupka, A., and Costa, P. J. M., 2019, Image analysis applied to quartz grain  
761 microtextural provenance studies: *Computers & Geosciences*, v. 125, p. 98–108.
- 762 Rose, C. V., Maloof, A. C., Schoene, B., Ewing, R. C., Linnemann, U., Hofmann, M., and  
763 Cottle, J. M., 2013, The End-Cryogenian Glaciation of South Australia: *Geoscience*  
764 *Canada*, v. 40, p. 256.
- 765 Runkel, A. C., Mackey, T. J., Cowan, C. A., and Fox, D. L., 2010, Tropical shoreline ice in the  
766 late Cambrian: Implications for Earth’s climate between the Cambrian Explosion and the  
767 Great Ordovician Biodiversification Event: *GSA Today*, p. 4–10.
- 768 Schelp, C., 2019, An Alternative Way to Plot the Covariance Ellipse, at CarstenSchelp.github.io  
769 at [https://carstenschelp.github.io/2018/09/14/Plot\\_Confidence\\_Ellipse\\_001.html](https://carstenschelp.github.io/2018/09/14/Plot_Confidence_Ellipse_001.html).
- 770 Setlow, L. W., 1978, Age determination of reddened coastal dunes in northwest Florida, U.S.A.,  
771 by use of scanning electron microscopy, *in* *Scanning electron microscopy in the study of*  
772 *sediments*: *Geo Abstracts*, p. 283–305.
- 773 Shacat, J. A., Green, W. J., DeCarlo, E. H., and Newell, S., 2004, The Geochemistry of Lake  
774 Joyce, McMurdo Dry Valleys, Antarctica: *Aquatic Geochemistry*, v. 10, p. 325–352.
- 775 Smith, C., Soreghan, G. S., and Ohta, T., 2018, Scanning electron microscope (SEM)  
776 microtextural analysis as a paleoclimate tool for fluvial deposits: A modern test: *GSA*  
777 *Bulletin*, v. 130, p. 1256–1272.

- 778 Spigel, R. H., and Priscu, J. C., 1998, Physical limnology of the McMurdo Dry Valleys Lakes, *in*  
779 Ecosystem Dynamics in a Polar Desert: the McMurdo Dry Valleys, Antarctica: American  
780 Geophysical Union, p. 153–187.
- 781 Stevic, M., 2015, Identification and environmental interpretation of microtextures on quartz  
782 grains from aeolian sediments - Brattforsheden and Vittskövle, Sweden [BS Thesis]:  
783 Lund University, 35 p.
- 784 Stokes, S., Kocurek, G., Pye, K., and Winspear, N. R., 1997, New evidence for the timing of  
785 aeolian sand supply to the Algodones dunefield and East Mesa area, southeastern  
786 California, USA: *Palaeogeography, Palaeoclimatology, Palaeoecology*, v. 128, p. 63–75.
- 787 Sweet, D. E., and Soreghan, G. S., 2010, Application of quartz sand microtextural analysis to  
788 infer cold-climate weathering for the equatorial Fountain Formation (Pennsylvanian-  
789 Permian, Colorado, U.S.A.): *Journal of Sedimentary Research*, v. 80, p. 666–677.
- 790 Sweet, D. E., and Brannan, D. K., 2016, Proportion of Glacially To Fluvially Induced Quartz  
791 Grain Microtextures Along the Chitina River, SE Alaska, U.S.A.: *Journal of Sedimentary*  
792 *Research*, v. 86, p. 749–761.
- 793 Vincent, P. J., 1976, Some periglacial deposits near Aberystwyth, Wales, as seen with a scanning  
794 electron microscope: *Biuletyn Periglacialny*, v. 25, p. 59–64.
- 795 Vos, K., Vandenberghe, N., and Elsen, J., 2014, Surface textural analysis of quartz grains by  
796 scanning electron microscopy (SEM): From sample preparation to environmental  
797 interpretation: *Earth-Science Reviews*, v. 128, p. 93–104.
- 798 Williams, G. E., 1998, Late Neoproterozoic periglacial aeolian sand sheet, Stuart Shelf, South  
799 Australia\*: *Australian Journal of Earth Sciences*, v. 45, p. 733–741.
- 800 Wilson, I. G., 1972, Aeolian bedforms—their development and origins: *Sedimentology*, v. 19, p.  
801 173–210.
- 802 Winspear, N. R., and Pye, K., 1995, Sand supply to the Algodones dunefield, south-eastern  
803 California, USA: *Sedimentology*, v. 42, p. 875–891.
- 804 Woronko, B., 2016, Frost weathering versus glacial grinding in the micromorphology of quartz  
805 sand grains: Processes and geological implications: *Sedimentary Geology*, v. 335, p.  
806 103–119.
- 807 Yu, W., Algeo, T. J., Du, Y., Zhou, Q., Wang, P., Xu, Y., Yuan, L., and Pan, W., 2017, Newly  
808 discovered Sturtian cap carbonate in the Nanhua Basin, South China: *Precambrian*  
809 *Research*, v. 293, p. 112–130.
- 810 Zhang, S., Jiang, G., and Han, Y., 2008, The age of the Nantuo Formation and Nantuo glaciation  
811 in South China: *Terra Nova*, v. 20, p. 289–294.